Marine Geology 492 (2026) 107697

Contents lists available at ScienceDirect

Marine Geology

journal homepage: www.elsevier.com/locate/margo

Research Article

Early Pleistocene (1.94–1.46 Ma) records for the upper Mediterranean Outflow Water branch reveal low and high latitude climate influences

Antje H.L. Voelker [a,b,*], Emanuelle Ducassou [c], Barbara Balestra [d,e], Jose Abel Flores [f], Gary D. Acton [g,1], Carl Richter [h], Chuang Xuan [i], Johanna Lofi [j], Ana Alberto [a,2], Henning Kuhnert [k], Carlos A. Alvarez Zarikian [g]

[a] Divisão de Geologia e Georecursos Marinhos, Instituto Português do Mar e da Atmosfera (IPMA), Avenida Dr. Alfredo Magalhães Ramalho 6, 1495-165 Algés, Portugal
[b] Centro de Ciências do Mar do Algarve (CCMAR/CIMAR LA), Campus de Gambelas, Universidade do Algarve, 8005-139 Faro, Portugal
[c] UMR 5805 EPOC, Université de Bordeaux, Allée Geoffroy Saint-Hilaire CS 50023, 33615 Pessac Cedex, France
[d] National Museum of Natural History (NMNH), Smithsonian, Paleobiology Department, Washington, DC 20560, USA
[e] American University, Department of Environmental Science, Washington, DC 20016, USA
[f] Departamento de Geología, Universidad de Salamanca, 37008 Salamanca, Spain
[g] International Ocean Discovery Program (IODP), Texas A&M University, 1000 Discovery Drive, College Station, TX 77845, USA
[h] School of Geosciences, University of Louisiana at Lafayette, 611 McKinley Street, Hamilton Hall #323, P.O. Box 44650, Lafayette, LA 70504, USA
[i] School of Ocean and Earth Science, National Oceanography Centre Southampton, University of Southampton, Waterfront Campus, European Way, Southampton SO14 3ZH, United Kingdom
[j] University of Montpellier, CNRS, Place E. Bataillon, 34095 Montpellier Cedex 05, France
[k] MARUM, Universität Bremen, Leobener Straße 8, 28359 Bremen, Germany

ARTICLE INFO

Editor: Michele Rebesco

Keywords:
IODP Expedition 339
Mediterranean Outflow Water
Early Pleistocene
Nannostratigraphy
Magnetostratigraphy
Contourite beds
Downhole logging

ABSTRACT

The Mediterranean Outflow Water (MOW), modified by paleoceanographic conditions and tectonic processes, played a significant role in the formation of sediments drifts along the Iberian Margin. Using sediment samples from IODP Hole U1387C, we explore the Early Pleistocene history of the upper MOW core above the central Faro Drift in the Gulf of Cádiz. The time series of benthic foraminifer stable isotope and grain size related data have a rigorous stratigraphic framework consisting of nannofossil biostratigraphy and paleomagnetic and $\delta^{18}O$ stratigraphy. The paleoenvironmental records are supplemented by natural gamma ray downhole logging data. Above the hiatus associated with the youngest dolostone, sandy to muddy contourite sedimentation started at 1.946 Ma, i.e., within Marine Isotope Stage (MIS) 74, at IODP Site U1387, slightly younger than at IODP Site U1389. Formation of contourite layers, reflected in the sortable silt and sand percentage records, strongly reacted to precession forcing, including semi- and quarter-precession cycles. The majority of the contourite beds developed during stadial (colder) climate periods, like previous observations from the Early to Late Pleistocene. Formation of contourite layers within MIS 53, MIS 55 and MIS 65, however, appear to be linked to the prevailing atmospheric conditions over North Africa. Periods of poor ventilation in the upper MOW were linked to insolation maxima and reduced ventilation in the Mediterranean Sea. Here, MIS 51 presents a peculiar case as poor ventilation reached from the surface to the lower North Atlantic Deep Water range, reflecting unique interglacial conditions that merit future exploration.

1. Introduction

The Early Pleistocene prior to the Early to Middle Pleistocene Transition (Head and Gibbard, 2015) belongs to the "41 kyr world" when obliquity controlled the timing of glacial-interglacial cycles (e.g., Hodell and Channell, 2016b; Huybers, 2007; Raymo and Nisancioglu,

* Corresponding author at: Divisão de Geologia e Georecursos Marinhos, Instituto Português do Mar e da Atmosfera (IPMA), Avenida Dr. Alfredo Magalhães Ramalho 6, 1495-165 Algés, Portugal.
E-mail address: antje.voelker@ipma.pt (A.H.L. Voelker).
[1] Now at: Retired, 1302 Caudill Street, College Station, TX 77840, USA.
[2] Now at: Instituto Dom Luiz (IDL), Faculdade de Ciências da Universidade de Lisboa, Campo Grande Edifício C1, Piso 1, 1749–016 Lisboa, Portugal.

https://doi.org/10.1016/j.margeo.2025.107697
Received 17 September 2025; Received in revised form 9 December 2025; Accepted 12 December 2025
Available online 13 December 2025

2003; Raymo et al., 2004) (following Aubry et al. (2009) we use Ma/ka when referring to a date and Myr/kyr when referring to duration/cycles). The glacial-interglacial cycles were more symmetrical than in the "100 kyr world" after the Early to Middle Pleistocene Transition and glaciations generally less intense (Maslin and Brierley, 2015). The Allan Hills blue-ice records from East Antarctica (Yan et al., 2019), although temporally restricted, recently confirmed this assumption: interglacial periods were not significantly warmer in the "41 kyr world" and had atmospheric CO_2 levels comparable to the Late Pleistocene, whereas glacial periods were less intense prior to the Early to Middle Pleistocene Transition and had atmospheric CO_2 levels around 24 ppm higher than during the Late Pleistocene. Soil carbonate derived CO_2 reconstructions even point to interglacial levels remaining below 300 ppm throughout the whole Early Pleistocene (0.9–2.6 Ma) (Da et al., 2019; The Cenozoic CO2 Proxy Integration Project Consortium et al., 2023), which agrees with boron isotope based evidence from the tropical Atlantic (Hönisch et al., 2009; Dyez et al., 2018; Nuber et al., 2025). A gradual cooling trend in the global mean surface temperatures started at 4 Ma and lasted until 1 Ma, although temperatures became more variable after 2 Ma and particularly after 1.5 Ma (Clark et al., 2024).

Time slice (10 kyr duration) reconstructions back to Marine Isotope Stage (MIS) 64 (last 1.8 Ma) indicate that the vertical water-mass structure in the subpolar North Atlantic did not differ significantly between the "41 kyr" world and the Middle-to-Late Pleistocene during both glacials and interglacials (Raymo et al., 2004). Records from intermediate depths (1150–2300 m), however, show lower $\delta^{13}C$ values during Early Pleistocene glacial intervals, which was attributed to a more extensive sea-ice cover in the Norwegian Greenland Sea as source region for that water mass (Raymo et al., 2004). The 3.2 Myr long and higher resolution benthic foraminifera isotope records from IODP Site U1308 (49°52.67′N, 24° 14.289′W; Fig. 1b) show, nevertheless, that the North Atlantic experienced mode changes related to the intensification of the northern hemisphere glaciation (Hodell and Channell, 2016b). Such mode transitions occurred at 2.7 Ma, 1.5 Ma, 0.9 Ma and 0.65 Ma and are related to an increasing vertical $\delta^{13}C$ gradient between intermediate and deep-water masses, implying changes in the carbon storage in the deep ocean and atmospheric CO_2 concentrations (Hodell and Channell, 2016b; Hines et al., 2024; Nuber et al., 2025). Between MIS 94 (~2.4 Ma) and MIS 52 (~1.54 Ma) glacial stages were generally weaker, in agreement with the atmospheric CO_2 evidence (The Cenozoic CO2 Proxy Integration Project Consortium et al., 2023). The amplitude of glacial-interglacial cycles increased from MIS 52 onwards (Hodell and Channell, 2016b), which coincides in general with the 1.5 Ma mode change. The mode change is observed throughout the Atlantic Ocean and associated with glacial shoaling of Northern Component Water and a lag in response of middle deep Atlantic (2300–4000 m) benthic $\delta^{13}C$ to

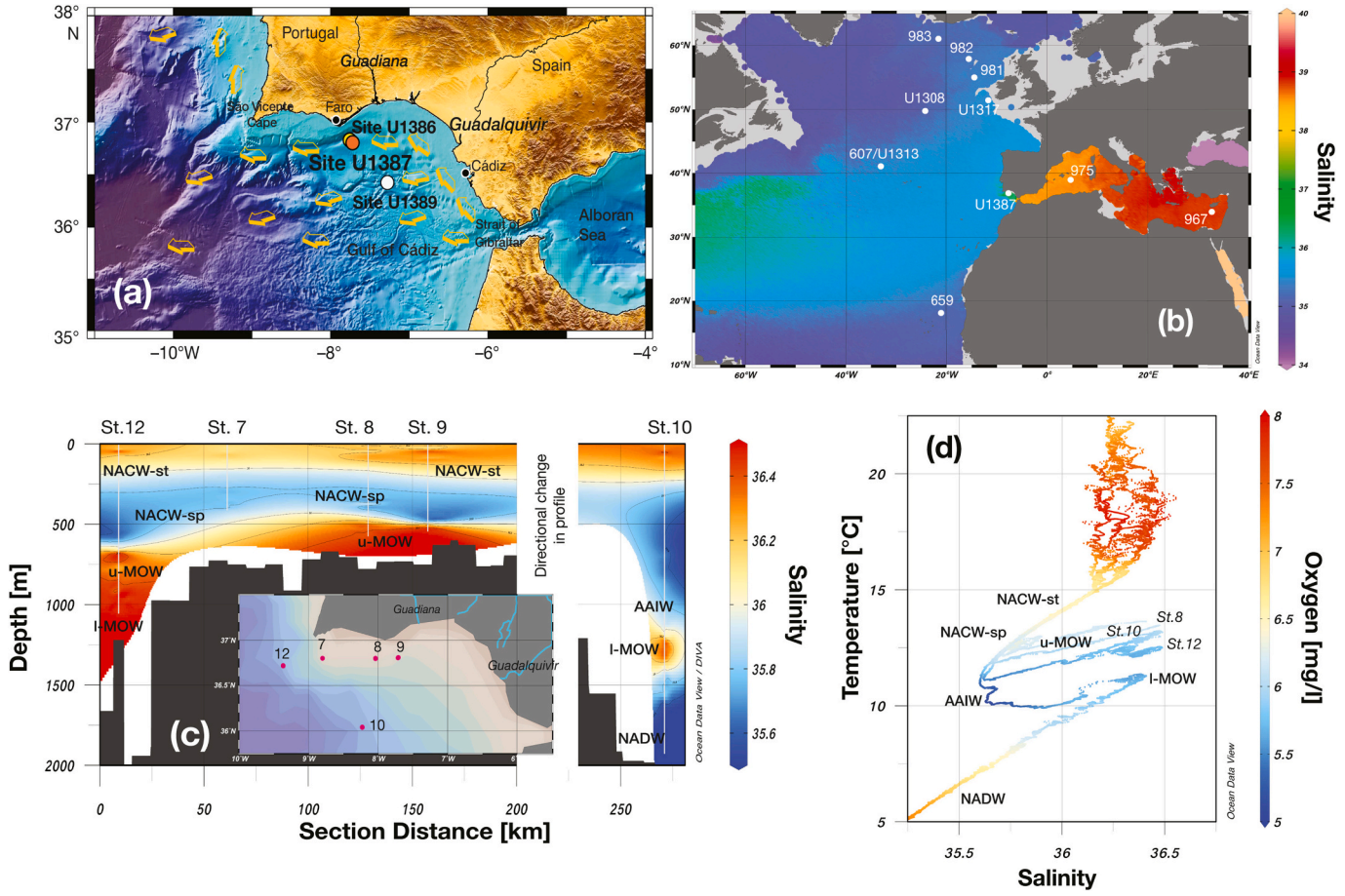

Fig. 1. a) Map of the SW Iberian margin with the locations of the IODP Expedition 339 Sites mentioned in the text. In the bathymetry colour scale, shades of blue become darker with increasing depth. Arrows indicate MOW flow paths. b) Map of the North Atlantic Ocean and Mediterranean Sea showing the location of sites mentioned in the text, with annual mean salinity at 560 m as background (World Ocean Atlas 2023, 0.25 degree resolution) (Reagan et al., 2024). c) Salinity profile along the Algarve margin and into the central Gulf of Cádiz based on CTD data collected at Iberia-Forams stations (St.) 12, 7 to 9 and 10 (see inserted map) in September 2012 (Voelker et al., 2015a; Voelker et al., 2015b). Lines at station numbering indicate real length of CTD profile. d) Salinity-temperature profiles and respective oxygen concentration for the five Iberia-Forams stations shown in b). Water masses are abbreviated in c) and d) as: AAIW – Antarctic Intermediate Water; MOW – Mediterranean Outflow Water with u = upper and l = lower; NACW – North Atlantic Central Water with sp. = subpolar and st = subtropical origin; and NADW – North Atlantic Deep Water. Basic maps (b, c) and plot (d) produced with the Ocean Data View software (Schlitzer, 2025). (For interpretation of the references to colour in this figure legend, the reader is referred to the web version of this article.)

orbital forcing (obliquity, precession) (Lisiecki, 2014). At the same time, but already starting around 1.6 Ma, εNd signals at intermediate depth (2000–2500 m) sites south of the Wyville Thomson Ridge (Rockall trough) point to a major weakening of deep-water production in the Nordic Seas, primarily during interglacials (Khélifi and Frank, 2014). The changes in the North Atlantic circulation gained influence on climate in the Mediterranean region between 2.2 and 1.2 Ma, when polar processes increasingly contributed to climate forcing in a combination with the regional forcing and processes that dominated until 2.2. Ma (Colleoni et al., 2012).

Sea-level related paleoclimate records (e.g., benthic $\delta^{18}O$) are clearly obliquity-paced during the late Pliocene to early Pleistocene and lack power in the precession spectrum. Raymo et al. (2006) postulated that the precession signal might be cancelled out due to the partially out-of-phase waxing and waning of the northern and southern hemisphere ice sheets, which was recently confirmed by Morée et al. (2021). In the Mediterranean Sea region, on the other hand, precession played an important role in modifying paleoclimate conditions throughout the Plio-Pleistocene, especially in relation to the strength of the African monsoon. Hydrological changes across northern Africa, as reflected in increased run-off from the Nile river (e.g., Castañeda et al., 2016; Emeis et al., 2003; Revel et al., 2010) or reduced Saharan dust flux (Larrasoaña et al., 2003), have been linked to the formation of the organic-rich sapropel layers in the eastern Mediterranean Sea (Emeis et al., 2000; Grant et al., 2022b; Rohling et al., 2015; Rossignol-Strick et al., 1982; Rossignol-Strick et al., 1998). Sapropel layers were dated assuming a temporal lag of 3000 years between the precession minimum (insolation maximum) and the mid-point of a sapropel layer (Hilgen et al., 1993; Lourens et al., 1996). The detailed sapropel history back to 5.3 Ma at ODP Site 967 in the eastern Mediterranean Sea (Fig. 1b) revealed, however, that not all sapropel layers were associated with an insolation maximum (Grant et al., 2022b). Precession-related strengthening of the hydrological cycle also affected the southern Iberian Peninsula (Bosmans et al., 2015b) and resulted in increased riverine input to sediments from the Gulf of Cádiz and the southwestern Iberian margin (Lofi et al., 2016; Sierro et al., 2000; Moal-Darrigade et al., 2022a). Furthermore, weakening of the overturning circulation in the Mediterranean Sea during times of sapropel formation was linked to changes in the characteristics of the Mediterranean Outflow Water (MOW) in the Gulf of Cádiz during the Early and Late Pleistocene, where those periods were associated with a more sluggish circulation (e.g., Bahr et al., 2015; Singh et al., 2015; Sierro et al., 2020; Voelker et al., 2015c; Voelker et al., 2022; Moal-Darrigade et al., 2022a; Moal-Darrigade et al., 2022b). On the other hand, higher MOW flow intensity has been proposed as cause for the formation of hiatuses (dolostones) in the Plio- to Pleistocene drift sequences along the southern and southwestern Iberian margin (Hernández-Molina et al., 2014). The younger hiatus, which shipboard biostratigraphic data suggest began earlier than 3.19 Ma and ended around 2 Ma (Stow et al., 2013), aligns with the onset of northern hemisphere glaciation and the first mode change in North Atlantic circulation (Hodell and Channell, 2016b). However, the onset of hemipelagic sedimentation following the hiatus appears to be time transgressive along the various MOW pathways (Kaboth et al., 2017b; Lebreiro et al., 2015).

The current study aims to decipher the Early Pleistocene (2.0- ~1.5 Ma) history of the MOW at Integrated Ocean Drilling Program (IODP) Site U1387 (36°48′N 7°43′W; 559 m water depth) (Fig. 1a) and to place the MOW signals into the context of northern hemisphere and regional Mediterranean/ NW African climate changes. To reconstruct MOW conditions, we use benthic foraminifer stable isotope and grain size records in combination with downhole logging data. The chronostratigraphy of the record is built on $\delta^{18}O$ stratigraphy supported by paleomagnetic and calcareous nannofossil biostratigraphic data to confirm the identification of MIS, in the lower part of the Site U1387 sedimentary succession where core recovery was poorer. Another objective is to determine the upper age boundary of the youngest of the two dolostone beds at Site U1387, marking the onset of sandier contourite deposition in Lithostratigraphic Unit IC at the Faro Drift (Expedition 339 Scientists, 2013b).

2. Regional setting

During IODP Expedition 339 – Mediterranean Outflow, Site U1387 was drilled into the Faro drift on the southern Portuguese margin (Stow et al., 2013). The mounded Faro Drift was built up since the Pliocene by activity of the upper MOW core (Roque et al., 2012; Hernández-Molina et al., 2014). The MOW (sometimes also called Atlantic Mediterranean Water) is the dominant water mass in the intermediate depths of the Gulf of Cádiz and along the western Iberian margin. Due to differential mixing between the warm, saline water exiting the Mediterranean Sea as deep overflow and the overlying, less dense eastern North Atlantic Central Water (NACW) (Fig. 1c, d), the MOW forms two branches: an upper branch centered between 500 and 800 m and a more saline, denser lower branch between 1000 and 1400 m (Ambar and Howe, 1979; Baringer and Price, 1997). Besides spreading out into the Gulf of the Cádiz, the branches flow mainly northwestward along the western Iberian margin (Fig. 1a, b). The upper MOW branch is about 50–60 m thick above the Faro Drift (Fig. 1c; location of Ib-F station 8 corresponds to Site U1387) and fills the moat that formed along the drift's northern edge (see Fig. 2 in Hernández-Molina et al., 2014). Between 750 and 1000 m, the MOW occupies the same depths as the Antarctic Intermediate Water (AAIW), which flows northward along the African continental margin and penetrates the Gulf of Cádiz from the southern to southeastern side, leading to mixing between the two water masses and entrainment of nutrients from the AAIW into the MOW (Cabeçadas et al., 2010; Louarn and Morin, 2011). Sometimes, remnants of AAIW can be observed in the Gulf of Cádiz (Cabeçadas et al., 2002; Cabeçadas et al., 2003; Voelker et al., 2015a), such as during the occupation of Iberia-Forams station 10 in the central Gulf of Cádiz (Fig. 1c, d). The MOW contains less oxygen than the surrounding North Atlantic water masses, but lowest oxygen levels are associated with the AAIW (Fig. 1d) (Cabeçadas et al., 2003; Cabeçadas et al., 2010). Roque et al. (2019) showed that AAIW prevails in the Gulf of Cádiz during the fall and then pushes the MOW towards the upper continental slope.

3. Material and methods

The sediment sequence recovered in Hole U1387C above the younger dolostone (457.3–458.0 m below sea floor (mbsf)) consists of sandy to muddy contourites interbedded with turbidites (Stow et al., 2013). While cores U1387C-2R to U1387C-8R-2 are part of the stratigraphic splice with Holes U1387A and B, the cores below section U1387C-8R-2 (below 357.52 mbsf equivalent to 394.69 m composite depth) are only appended to the splice (Expedition 339 Scientists, 2013b). Naturally, there are coring gaps within the single cored interval below core U1387C-8R.

This study focuses on the sediments from the top of core U1387C-8R to the top of the youngest dolostone near the bottom of section U1387C-19R-3. Since we are working exclusively with Hole U1387C sediments and to facilitate comparison to the downhole logging data, we are using the *Core depth below Sea Floor* (CSF) depth scale instead of the composite depth scale of the splice (https://www.iodp.org/policies-and-guidelines/142-iodp-depth-scales-terminology-april-2011/file). Thus, sedimen t-sample derived parameters are presented on CSF-B (in mbsf), which, as a compression-scaled version of CSF-A, allows correcting for overlapping sediments if core recovery was above 100 %. The conversion to CSF-B was needed to accommodate overlapping CSF-A depths at the transition from core U1387C-8R-CC to core U1387C-9R-1.

3.1. Sample preparation

The Portuguese sample series, which combines samples from several

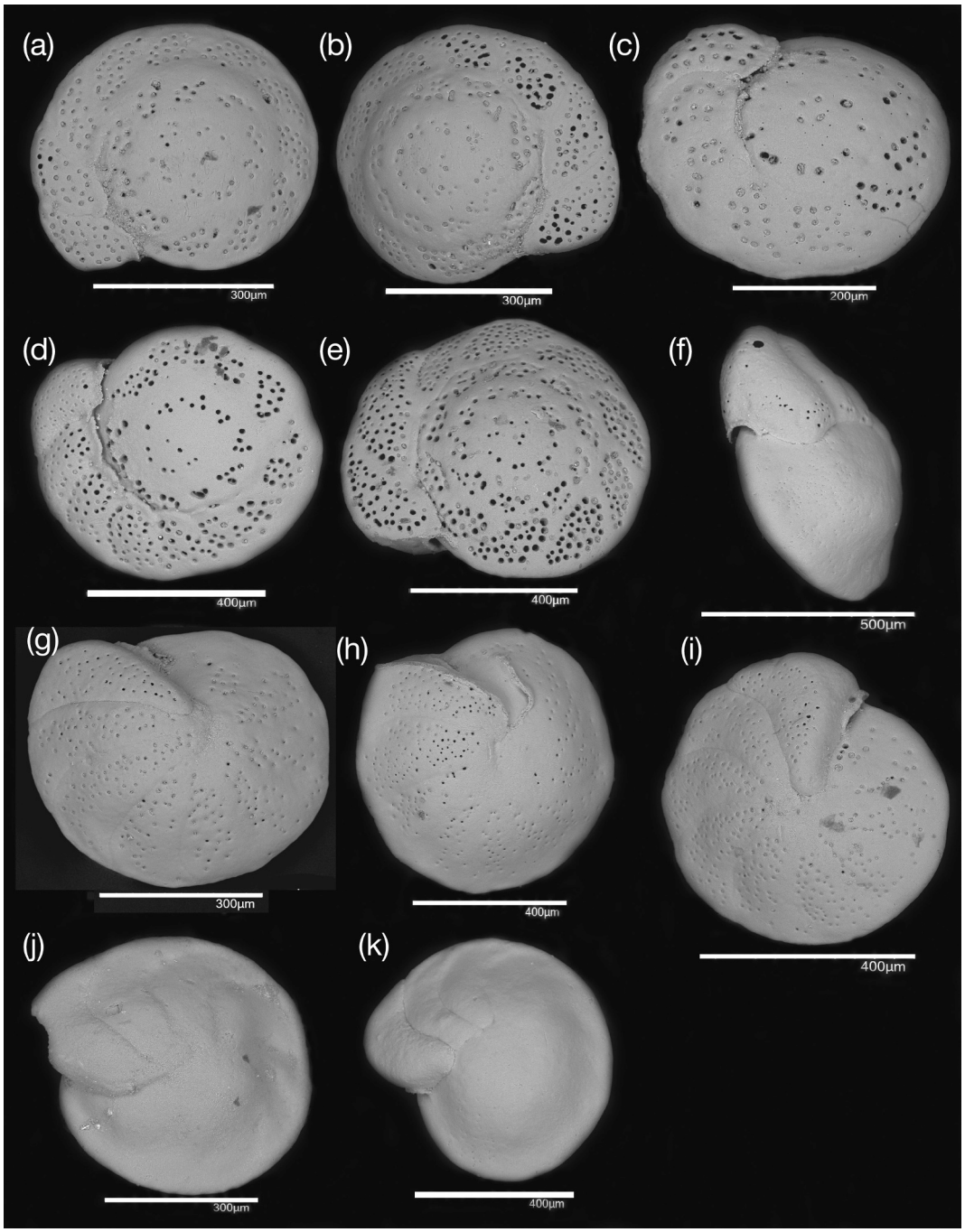

Fig. 2. Scanning electron microscope (Hitachi TM 4000 Plus) pictures of the regional morphological variant of *Cibicides pachyderma*. a) to e) spiral views; g) to i) umbilical (dorsal) views. f), j) and k) umbilical views of the more typical *Cibicides pachyderma* variant with hardly any perforation and the distinct peripheral band (rim). Specimens are from samples: a) U1387C-12R-5124–126 cm; b) and g) U1387C-12R-6 14–16 cm; c) and j) U1387C-15R-2122–124 cm; d), f), and k) U1387B-33X-2 2–4 cm; e) and h) U1387B-28X-2 2–4 cm; i) U1387C-12R-7 43–45 cm.

requests by researchers from the Instituto Português do Mar e da Atmosfera (IPMA) taken from the working halves, covers the interval from U1387C-8R-1 4–6 cm to U1387C-19R-3131–133 cm (347.64–457.31 mbsf). As part of the splice, the average sample resolution within core U1387C-8R is 12.5 cm (15–30 cc sample volume), conforming with the Middle to Early Pleistocene time series of Site U1387 (Voelker et al., 2015c; Voelker et al., 2018). Below core U1387C-8R, the resolution of the initially, evenly spaced 45 cm resolution series (15 cc volume) was increased in 2016. The additional samples with a 30 cc volume were taken by the staff of the Bremen Core Repository (BCR) at pre-described depths (avoiding biscuit transitions) and increased the sample resolution to an average of 15 cm, including core catcher (CC) sections. All samples from the 2016 series were subsampled for calcareous nannofossil studies.

The sediment samples were prepared following the procedure established in the Sedimentology and Micropaleontology Laboratory of the IPMA's Marine Geology Division (DivGM). The samples were weighed, frozen, freeze-dried, and weighed again to obtain a wet and a dry weight, respectively. The dried sediment material was then washed through a 63 µm-mesh screen to separate the sand fraction >63 µm from the finer sediments. The sand fraction was dried at 40 °C and weighed. The relationship between the weight of the sand fraction and the dry

weight yields the weight-percent (wt%) sand value that can be used as a rough indicator for contourite beds (Voelker et al., 2015c; Voelker et al., 2022).

Additional samples from sections U1387C-18R-5 to U1387C-19R-3 from the lower resolution sample series of C. Alvarez Zarikian (average sample spacing 0.61 m) were used only for the stable isotope study. These samples were processed at TAMU (College Station) following the same preparation procedure as for the Portuguese sample series except that the wet bulk samples were not weighted before being frozen and freeze-dried.

3.2. Stable isotope analyses

The stable isotope study included all dried sand fraction samples from the Portuguese sample series and those from sections U1387C-18R-5 to U1387C-19R-3 in the sample series of C. Alvarez Zarikian. For analyzing the stable isotope values in benthic foraminifer shell carbonate, 2 to 7 clean specimens of the species *Cibicides pachyderma* or *Planulina ariminensis* were collected from the fraction >250 μm. Some of the *Cibicides pachyderma* specimens represent a regional morphological variant (personal communication J. Schönfeld, October 2018) that is generally smaller than the typical *C. pachyderma* variant, often perforated on the umbilical (dorsal) side and exhibits no clearly defined peripheral band at the periphery (Fig. 2). In five samples, none of those species were available and shells of *Uvigerina* spp., most likely specimens of *Uvigerina peregrina parva* (Schönfeld, 2006; Schönfeld and Altenbach, 2005), were analyzed instead. Combining the *Cibicides* and *Planulina* data to one continuous record followed Voelker et al. (2015c), whereby the $\delta^{18}O$ values of both species remain uncorrected (Marchitto et al., 2014) and the $\delta^{13}C$ values of *C. pachyderma* are adjusted to the *P. ariminensis* level by adding 0.3 ‰. Because the analysis of *Uvigerina* spp. specimens was limited to five samples, these data are incorporated into the combined record by subtracting 0.64 ‰ from the *Uvigerina* $\delta^{18}O$ values (i.e., correction to *Cibicidoides* level, contrary to the more common correction of *Cibicidoides* to the *Uvigerina* level; Shackleton (1974)). The *Uvigerina* $\delta^{13}C$ values were not integrated but are archived together with the other isotope data at the World Data Center PANGAEA (Felden et al., 2023).

The stable isotopes analyses were performed at MARUM (University Bremen, Germany) using a Finnigan MAT 251 mass spectrometer that is coupled to an automated Kiel I carbonate preparation system. The mass spectrometer's long-term precision is ±0.05 ‰ for $\delta^{13}C$ and ± 0.07 ‰ for $\delta^{18}O$ based on repeated analyses of in-house (ground Solnhofen limestone) and external (NBS-19) carbonate standards.

3.3. Sample series for grain-size analysis

For grain-size analysis an additional sample series with a 10 cc volume was taken to understand the sedimentological changes at Site U1387, in particular the nature of the contourite beds. With focus on the contourite beds, higher sample resolution (one every 10 cm interval) occurs in the sandier intervals, whereas resolution drops to one sample every ≥30 cm (up to 150 cm) in the finer-grained intervals (Fig. 3). The series includes samples from core sections U1387C-8R-1100 cm to U1387C-19R-3133 cm (348.60–457.33 m). The samples were prepared for grain size analysis, without removing the carbonates, and measured with the Malvern Mastersizer S laser microgranulometer (Malvern Panalytical, Malvern, UK), at the EPOC laboratory, University of Bordeaux (France). Results for the grain size range from 0.02 to 2000 μm are reported as % sand, % silt and % fine fraction <10 μm of each sample, respectively. In addition, D90 (meaning that 90 % of the sediment is below this grain size value) and Sortable Silt ($\overline{SS}$; McCave, 2023) values were calculated.

3.4. Calcareous nannofossil biostratigraphy

The shipboard nannofossil biostratigraphy (Expedition 339 Scientists, 2013b) was refined based on 1) the shipboard smear slides prepared for those samples taken between the CC samples or 2) slides prepared from subsamples of the 2016 stable isotope sample series (Portugal samples). The additional shipboard samples average one sample per core section, whereas the resolution for the subsamples varies between one sample every 15 cm to every 30 cm. Slides for the calcareous nannofossil counts were prepared at the University of Salamanca following the method of Flores and Sierro (1997). The calcareous nannofossils were identified using standard light microscope techniques on a Zeiss Axiophot and with a polarizing microscope Leica DMRP at ×1250 and ×1000 magnification and a minimum of 200 fields of view in cross-polarized and plane-transmitted light (Balestra et al., 2019). Following Raffi et al. (2006) we use the terms Highest Occurrence (HO) and Lowest Occurrence (LO) to denominate biohorizons.

3.5. Paleomagnetism

During Expedition 339, continuous paleomagnetic measurements were made every 5 cm along the archive-half core sections using the shipboard cryogenic magnetometer (2G Enterprises Model-760R). The natural remanent magnetization (NRM) was measured before and after progressive alternating field (AF) demagnetization with peak fields of 10 and 20 mT. The NRM data were cleaned by removing results from disturbed intervals and from near the ends of the core sections that are subject to edge effect. The cleaned data are available in Table T16 of Expedition 339 Scientists (Expedition 339 Scientists, 2013b) and the raw data are available online from the IODP LIMS Database. Hole U1387C was cored with the Rotary Core Barrel (RCB) system, which imparted only a weak drilling overprint, most or all of which was removed with AF demagnetization with low peak fields.

To permit more detailed demagnetization experiments, remove

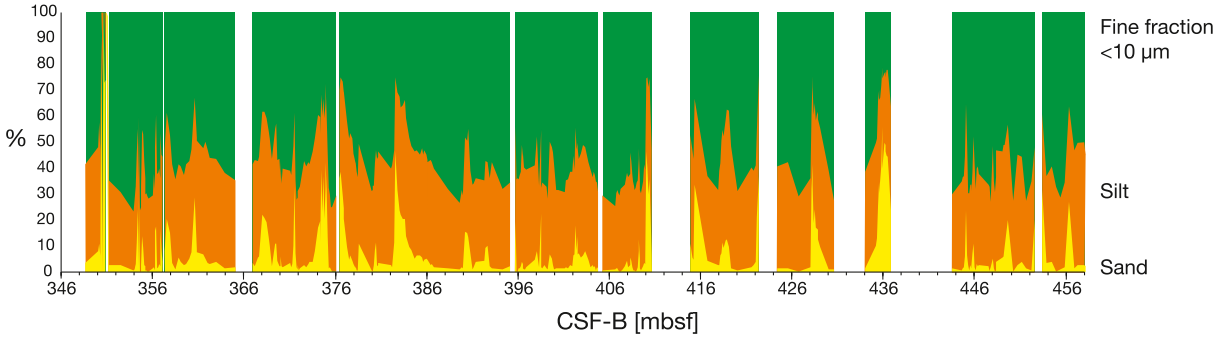

Fig. 3. Distribution and grain size profiles of samples from Cores U1387C-8R to U1387C-19R analyzed in the Malvern Mastersizer at the University Bordeaux. Note the varying sample resolution with higher resolution in sandier core intervals.

overprints more completely, and assess the characteristic remanent magnetization (ChRM) directions, oriented discrete sediment samples were collected by inserting a hollow extruder into the middle of working-half, split-core sections and then extruding the sediment into plastic cubes (2 cm × 2 cm × 2 cm, with an internal volume of ~7 cm^3) as described in Expedition 339 Scientists (2013a). We took one sample per section from Cores U1387C-7R to U1387C-61R (339–864 mbsf), which together provided roughly continuous 1.5-m spacing of samples over the entire cored interval. Another 12 samples were collected in 2016 by the BCR staff from Core U1387C-10R in an attempt to identify the Gilsa Excursion (Channell et al., 2016). In total, 75 discrete samples were evaluated within the interval of interest for this study (340–460 mbsf) (Fig. 4; Supplementary table 1).

Only five of these samples were measured during Expedition 339. Another 58 samples were measured post-cruise in the Paleomagnetism Laboratory at University of California-Davis and the 12 samples taken at the BCR were measured in laboratories at Sam Houston State University (SHSU), University of Houston (UH), and Tongji University (TU) (for details see identification in column AA = Measured in Supplementary table 1). NRM of the discrete samples were measured before and after progressive AF demagnetization with peak fields up to 100 mT at 5 to 10 mT steps. Paleomagnetic directions were determined from principal component analysis (PCA) (Kirschvink, 1980) using the ZPLOTIT software (Acton, 2011). Typically, the remanence measurements from at least five demagnetization steps for each interval were fit to lines using steps between 20 and 60 mT. PCA lines were fit using both the FREE option, in which the line is not required to pass through the origin of the plot, and the ANCHORED option, in which line is anchored to the origin. A Fisherian mean direction was also computed from the highest several demagnetization steps to estimate a stable end point (SEP).

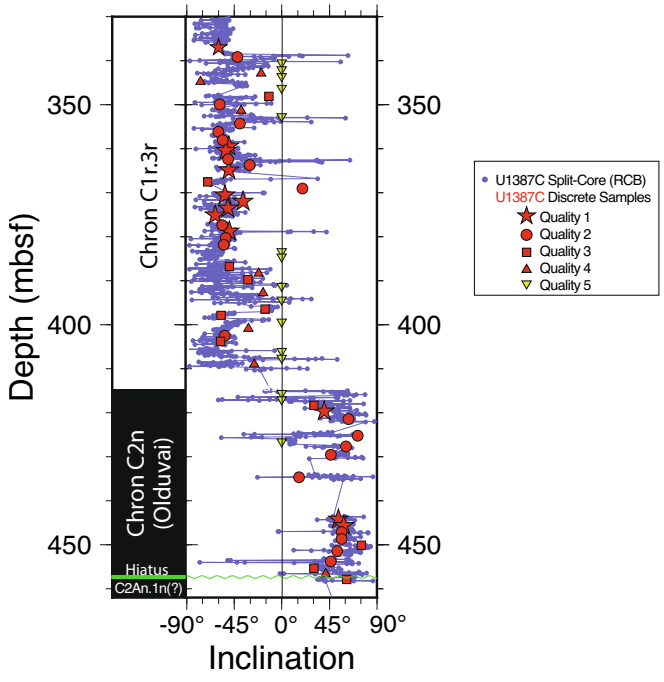

Fig. 4. Magnetic polarity (left column) and inclinations obtained for shipboard (blue dots and lines) and shorebased measurements in the interval of interest of Hole U1387C. For the discrete samples, inclination is plotted for the preferred inclination with the respective symbol highlighting the quality of the value (see legend on right). Quality scale ranges from 1 to 5 (as described in the "Material and Methods" section; Supplementary table 1) with 1 being the highest and 5 the lowest quality, the latter of which are plotted at 0° inclination merely to indicate the respective sample's depth. (For interpretation of the references to colour in this figure legend, the reader is referred to the web version of this article.)

For each sample, we determined a preferred inclination from the PCA FREE, PCA ANCHORED, or SEP estimate of the ChRM. The selection of which method best resolved the ChRM was based on visual inspection of the sample directions plotted on orthogonal vector diagrams (modified Zijderveld plots) and stereonets. The results for each sample were ranked with a quality factor (1 to 5), where Quality 1 was reserved for samples that displayed very linear decay of magnetization during demagnetization as noted by PCA maximum angular deviation (MAD) angles <5. Quality 2 are similar to Quality 1 but the MAD angles are between 5° and 10°. These highest quality (1 and 2) samples have very well resolved ChRM directions, and the polarity can be determined with great confidence. Quality 3 samples displayed moderate directional scatter during AF demagnetization, but a relatively noisy ChRM can be determined from which the polarity can be established. Quality 4 samples have large directional scatter during AF demagnetization and generally a significant drilling overprint that overlaps much of the coercivity spectra of the ChRM. The ChRM cannot be accurately determined although it is often possible to determine the polarity of these samples because they trend towards positive (normal polarity) or negative (reverse polarity) inclinations as they are demagnetized above about 40–80 mT. Quality 5 samples have such highly variable directions during AF demagnetization or are so strongly overprinted that their polarity is indeterminate. Of the 75 samples analyzed, 14 were quality 1, 20 were quality 2, 20 were quality 3, 8 were quality 4, and 13 were quality 5 (Fig. 4).

3.6. Downhole logging

After completion of coring operations at Hole U1387C, downhole logs were acquired with Schlumberger logging tools down to 649 mbsf (Expedition 339 Scientists, 2013a). The log data are measured in situ and continuously with depth, which results in the wireline-log depth scale expressed in meters wireline-log depth below seafloor (mwsf). In this paper, we focus on the natural gamma radiation (HSGR, standard total Gamma Ray) data that was acquired with the Hostile Environment Natural Gamma Ray Sonde (HNGS) of the triple combo tool string (Expedition 339 Scientists, 2013b). The HSGR log was acquired at a sampling interval of 15.24 cm (6 in.) and with an approximate vertical resolution of 20–30 cm. As shown in Lofi et al. (2016), variations in HSGR reveal changes in the sedimentology with some low GR values indicating more coarser-grained levels.

3.7. Spectral analysis

To explore the cycles driving the different climatic signals and their temporal evolution we performed wavelet analysis on the unequal spaced time series (Foster, 1996) using the wavelet program embedded in the PAST statistic software package (version 4.11) (Hammer et al., 2001).

4. Stratigraphy and age models

4.1. Magnetostratigraphy and calcareous nannofossil biostratigraphy

The shipboard chronostratigraphic data provided only three age control points for the interval between U1387C-8R and U1387C-18R, i.e., two nannofossil datums and the Matuyama-Olduvai polarity transition (Expedition 339 Scientists, 2013b). The two calcareous nannofossil events were the LO of large *Gephyrocapsa* spp. (>5.5 μm) (1.61 Ma) and the HO of *Calcidiscus macintyrei* (1.66 Ma), which were both placed between samples U1387C-7R-CC and U1387C-8R-CC at 351.62 mbsf.

The Matuyama-Olduvai (C1r.3r/C2n) polarity transition was estimated by Expedition 339 Scientists (2013a) to be at ~412.5 mbsf based on split-core data from Hole U1387C. This agrees well with the new discrete data (Fig. 4), although the higher quality discrete results are too widely spaced to refine the location of the reversal. The reversal could be

anywhere between discrete samples U1387C-15R-3 48 cm at 418.28 mbsf and U1387C-14R-3 81 cm at 409.10 mbsf, with a mid-point at 413.69 mbsf. For the split core data, samples recording the reverse polarity Chron C1r.3r extend to the base of Core U1387C-14R and possibly down to Interval U1387C-15R-1 45 cm (Fig. 4). The inclinations for the upper 45 cm of Core U1387C-15R are, however, variable and may just be noise within the top of the core. For these reasons, we think the reversal can only be constrained to fall between the last split-core measurement near the base of Core U1387C-14R in Interval U1387C-14R-4 65 cm (410.35 mbsf) and Interval U1387C-15R-1 45 cm (415.25 mbsf), which is the first normal polarity direction (positive inclination) downhole that is preceded by a long sequence of other positive inclinations. The mid-point for the split-core data at 412.8 mbsf is the best estimate for the reversal. Both it and the mid-point for the discrete samples falls within the ~5-m coring gap between Cores U1387C-14R and 15R (Fig. 5). The reversal could be placed anywhere within this gap or even somewhere within the upper 45 cm of Core U1387C-15R.

The lower 40 m above the youngest dolostone can therefore be attributed to the Olduvai subchron (C2n) with an age of 1.945–1.778 Ma (Ogg, 2012). More recently, the timing of the top of the Olduvai has been defined with a radiogenic age of 1.787 ± 0.015 Ma and occurring during MIS 63 in many marine records (Channell et al., 2020). In Hole U1387C, the coring gap between Cores U1387C-14R and U1387C-15R occurs above MIS 61 in the oxygen isotope stratigraphy (see section 4.2), whereas the last normal discrete samples coincide with the transition from MIS 62 to MIS 61 (Fig. 5). This discrepancy between the $\delta^{18}O$ and paleomagnetic stratigraphies indicates that the age model in these cores should be treated with caution and might be revised in the future, when new data either from Site U1387 or the Sites recently drilled during IODP Expeditions 397 and 401 (Hodell et al., 2024; Flecker et al., 2025) become available.

The normal inclination value for the discrete sample at 369.05 mbsf is considered to be an outlier rather than representing the Gilsa excursion (see Supplementary table 1), which has been dated at the MIS 54/55 boundary (1.584 Ma) in the North Atlantic record of IODP Site U1308 (Channell et al., 2016).

The refined calcareous nannofossil biostratigraphy in the Early Pleistocene section of Hole U1387C (Balestra et al., 2019) places the HO of *Discoaster brouweri* between samples U1387C-19R-2 88–90 cm and U1387C-19R-2 14–16 cm (455.38–454.63 mbsf) (Fig. 5). Age ranges for the biohorizon span from the middle of MIS 77 to late MIS 73 (Raffi et al., 2006). Based on the oxygen isotope stratigraphy (see section 4.2) the event occurred during late MIS 73 with an age of 1.93 Ma (Table 1), in agreement with the Geological Time Scale (GTS) 2012 (Anthonissen and Ogg, 2012).

The newly identified biohorizon marking the LO of medium-sized *Gephyrocapsa* (> 4 μm) was located between samples U1387C-14R-1 88–90 cm and 80–82 cm, (406.08–405 mbsf). However, this event should be interpreted with caution due to the irregular and intermittent

Table 1
Calcareous nannofossil biostratigraphic and magnetostratigraphic markers.

Event	Mean depth in U1387C [mbsf]	Age in U1387C [Ma]	GTS2012 age [Ma]
LO of large *Gephyrocapsa* spp. (>5.5 μm)	368.07	1.545	1.62ˆ
HO of *Calcidiscus macintyrei*	378.21	1.579	1.60
HO of medium *Gephyrocapsa* spp. (>4 μm)	405.54	1.689	1.73
Matuyama-Olduvai (C1r.3r/C2n) polarity transition	415.59*	1.72	1.778
HO of *Discoaster broweri*	455.00	1.93	1.93

HO/LO: highest/lowest occurrence; * depth refers to last discrete sample with normal polarity and good MAD quality; ˆ1.59 Ma in GTS2020 (Raffi et al., 2020).

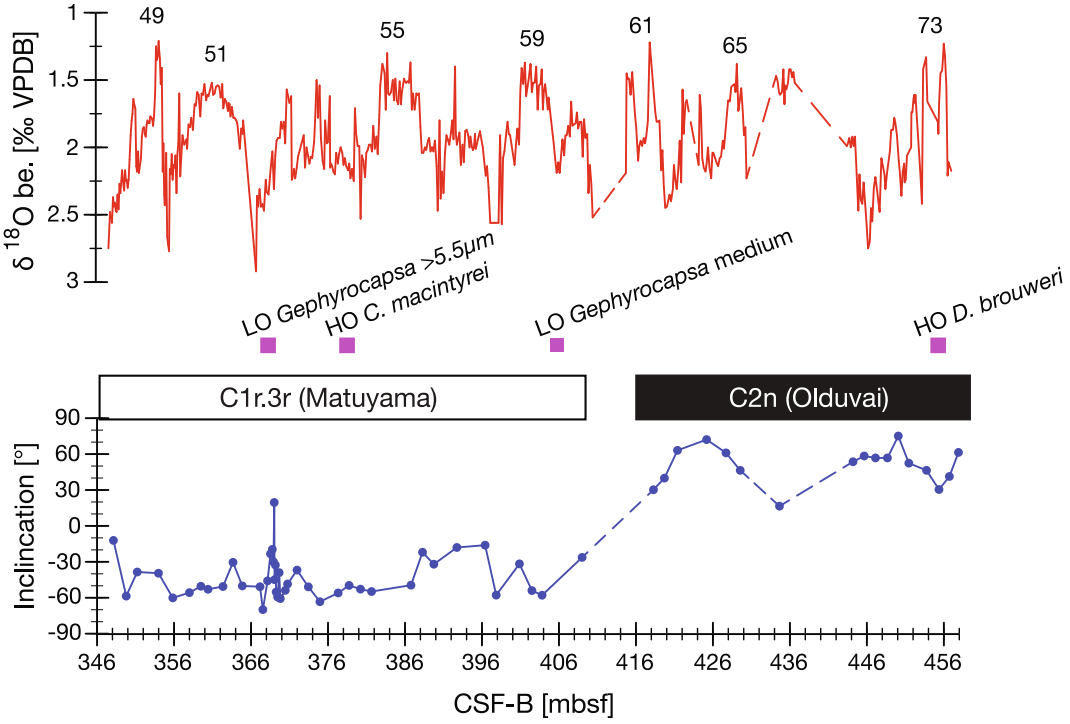

Fig. 5. Nannofossil and magnetostratigraphic evidence in Hole U1387C between 346 and 458 mbsf in comparison to the benthic $\delta^{18}O$ record (numbers above indicate some MIS). Magenta colored squares mark the depths of the respective nannofossil stratigraphic event with LO/FO indicating the first/last occurrence of the coccolithophore species. Bottom panel shows the identified magnetic polarity zones and the preferred inclinations for the discrete samples with qualities between 1 and 4 (see Fig. 4 for details). Dashed lines marked major coring gaps. (For interpretation of the references to colour in this figure legend, the reader is referred to the web version of this article.)

record, that could be also related to potential carbonate dissolution (Balestra et al., 2019). In Hole U1387C, the LO of medium-sized *Gephyrocapsa* occurred during MIS 59 (Fig. 5), which aligns well with its expected timing between MIS 59 and MIS 61 (Raffi et al., 2006). The age assigned to this biohorizon at IODP Site U1387 is 1.69 Ma (Table 1), consistent with its occurrence in the South Atlantic. However, this is slightly younger than its recorded age in the Mediterranean Sea (1.73 Ma) (Anthonissen and Ogg, 2012).

The HO of *Calcidiscus macintyrei* was identified between samples U1387C-11R-2 48–50 cm and U1387C-11R-2 14–16 cm (378.38–378.04 mbsf). That depth coincides with the MIS 54/ MIS 55 transition (Fig. 5), in agreement with the biohorizon's upper boundary indicated by Raffi et al. (2006) and the event's definition within the upper MIS 55 in the GTS2020 (1.6 Ma; Raffi et al., 2020). The LO of large *Gephyrocapsa* spp. (>5.5 μm) was placed between samples U1387C-10R-1 75–77 cm and U1387C-10R-1 48–50 cm (367.55–367.28 mbsf) (Fig. 5). Based on the $\delta^{18}O$ isotope stratigraphy that depth falls within MIS 52 (Fig. 5). Therefore, at Site U1387 the event occurred slightly higher (younger age) than the LO between MIS 55 and MIS 53, but lower (older age) than the lowest common occurrence (LCO) within MIS 48 (Raffi et al., 2006). The age corresponding to the LO of large *Gephyrocapsa* spp. (>5.5 μm) at Site U1387 is 1.545 Ma (Table 1), i.e. notably younger than the age assigned in the shipboard stratigraphy and in the GTS2012 (1.62 Ma; Anthonissen and Ogg, 2012) or the revised 1.59 Ma in the GTS2020 (Raffi et al., 2020).

4.2. Oxygen isotope stratigraphy and age models for IODP Sites U1387 and U1389

Using the nannofossil and magnetic stratigraphies as framework, the different MIS revealed in the benthic foraminifer $\delta^{18}O$ record of IODP Site U1387 are identified by comparison to the high-resolution benthic foraminifer $\delta^{18}O$ record of IODP Site U1308 (Hodell and Channell, 2016a; Hodell and Channell, 2016b) (Fig. 6). The alignment in the MIS 49 to MIS 65 interval was obvious as the great similarities in the shape of MIS 51, MIS 61 and MIS 65 provided solid anchor points. Due to the significant coring gaps below MIS 65 stratigraphic identification was more difficult. Since the magneto- and calcareous nannofossil stratigraphies specified that the sediments above the youngest dolostone were deposited during the Olduvai subchron, the low $\delta^{18}O$ values in the Site U1387 record below MIS 65 were associated with MIS 73 (Fig. 6). Although the millennial-scale oscillations during MIS 72 are not seen in the Site U1308 benthic foraminifer $\delta^{18}O$ record, they correspond with the oscillations recorded in the *Globigerina bulloides* $\delta^{18}O$ record of IODP Hole U1317E on the Irish margin (Fig. 1b) (Sakai et al., 2009). The assignment of the floating segment between MIS 65 and MIS 71 to the interval of MIS 67-MIS 69 was based on the record's shape and keeping the average sedimentation rates before and after in mind.

Transferring the LR04 chronology onto the Site U1387 record was subsequently obtained by aligning the benthic foraminifer $\delta^{18}O$ records of Sites U1387 and U1308 (Fig. 6), the latter of which was tuned to the LR04 stack (Hodell and Channell, 2016b). Initial tuning points were set at glacial maxima and/or glacial/interglacial transitions, whereas subsequent alignments were used to adjust clear offsets between the records. For the interval of MIS 48 to late MIS 49 the age model follows Voelker et al. (2022), although with the age control points transferred to the CSF-B scale, leading to a small age offset relative to Voelker et al. (2022) for the same sample. The resulting linear sediment rates vary between 3.8 cm/kyr and 45.6 cm/kyr with lower sedimentation rates commonly occurring during colder (glacial, stadial) climate phases (Fig. 6).

For directly comparing the benthic foraminifer isotope records of Sites U1387 and U1389, the Site U1389 data needed to be transferred from the MedStack chronology of Kaboth et al. (2017b) to the LR04 chronology. This was achieved by correlating the Site U1389 benthic $\delta^{18}O$ record (Kaboth et al., 2017c) to the one from IODP Site U1308 (Hodell and Channell, 2016b) (Supplementary Fig. S1). Identification of the MIS for the alignment followed Kaboth et al. (2017b) (note that MIS 73 was mislabeled as MIS 71 in Fig. 3 of Kaboth et al., 2017b), except for the interval of MIS 75 to MIS 77 where the broad $\delta^{18}O$ minimum at the beginning of the record was identified as MIS 77. Additional significant age shifts occur in the MIS 66 to MIS 69 interval (Supplementary Fig. S1). The chronology of the planktonic $\delta^{18}O$ record of western Mediterranean Sea ODP Site 975 (Fig. 1b) (Pierre et al., 2020; Pierre

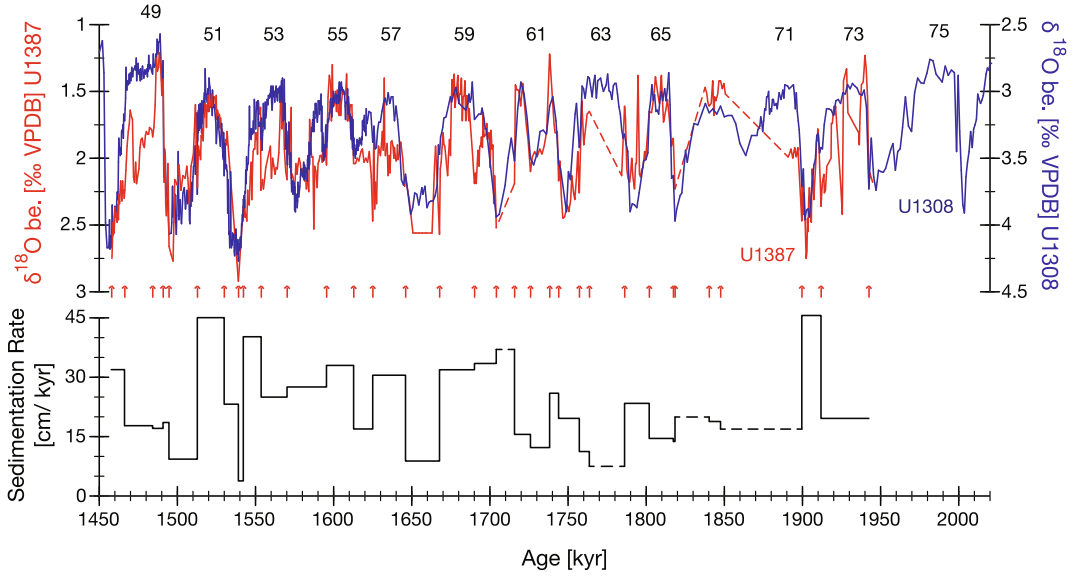

Fig. 6. Oxygen isotope stratigraphy, age model and sedimentation rates for the early Pleistocene sequence of Hole U1387C. Identification of particular MIS (interglacial MIS indicated by numbers) and an age model related to the LR04 stack (Lisiecki and Raymo, 2005) were obtained by tuning the Site U1387 benthic $\delta^{18}O$ record (red) to the one of IODP Site U1308 (blue) in the NE Atlantic (Hodell and Channell, 2016a; Hodell and Channell, 2016b). Tuning points, and thus age control points for Site U1387, are indicated by the arrows below the curves, whereby MIS transitions were primary tuning targets and additional points were set to adjust significant offsets resulting from extrapolation between the primary tuning points. The ensuing linear sedimentation rates for Site U1387 are shown in the bottom panel. Dashed lines indicate intervals of major coring gaps. (For interpretation of the references to colour in this figure legend, the reader is referred to the web version of this article.)

et al., 1999) was also adjusted to the LR04 chronology by correlating glacial maxima in the Site 975 data with maxima in the Site U1308 record. To minimize age offsets when comparing records, data from ODP Sites 607, 659 (only Tiedemann et al. (1994) data) and 981 were transferred to their respective LR04 chronology (Lisiecki and Raymo, 2005; http://www.lorraine-lisiecki.com/stack.html).

5. Results

5.1. Stable isotope data and respective spectral analysis results

The benthic foraminifer $\delta^{18}O$ record clearly shows glacial/interglacial cycles (Fig. 6, 7a) with higher values indicating glacial and stadial periods, concordant with reconstructions in younger periods of the Exp. 339 Sites (e.g., Bahr et al., 2015; Voelker et al., 2015c; Kaboth et al., 2016; Sierro et al., 2020). The benthic foraminifer $\delta^{13}C$ record indicates several minima with the more pronounced occurring at the beginning of interglacials MIS 61, MIS 57, MIS 51 and MIS 49 (Fig. 7b). Whereas the isotopic values of sample U1387C-16R-2 67–69 cm (426.47 mbsf) were determined as reworked and have been discarded from the data series, two other samples with very low $\delta^{13}C$ values were kept, but are flagged as potentially reworked. In both cases, samples U1387C-16R-3142–144 cm (428.72 mbsf) and U1387C-17R-1142–144 cm (435.32 mbsf), their $\delta^{18}O$ values fit the trends in the surrounding samples, whereas the corresponding $\delta^{13}C$ values do not. Flagging of sample U1387C-16R-3142–144 cm (428.72 mbsf) is further indicated due to the occurrence of turbidites within this core section (Alonso et al., 2016; B. Alonso, personal communication in 2016). On the other hand, the high $\delta^{13}C$ value of sample U1387C-15R-4 30–32 cm (419.60 mbsf) is perceived as valid because the corresponding $\delta^{18}O$ value falls within the general trend of the curve (Fig. 7).

Like other records from the deep Atlantic Ocean (Morée et al., 2021; Raymo et al., 2006), the Site U1387 benthic foraminifer $\delta^{18}O$ record is mainly showing power in the obliquity bandwidth (41 kyr cycles) (Fig. 8a). The spectral analysis of the benthic foraminifer $\delta^{13}C$ record, on the other hand, reveals a transition from obliquity in the earlier (older) part (1.7–1.78 Ma) towards precession in the younger part (1.5–1.65 Ma), whereby the precession signal is shifted towards the 23–25 kyr band (Fig. 8b).

5.2. Sedimentological and logging data and respective spectral analysis results

The Malvern derived wt% sand record generally agrees well with the wt% sand data obtained from the wet sieved samples (Fig. 7g). The exception is the interval between 350.41 and 351.09 mbsf (within late MIS 49) when the Malvern data indicates dominant sand contributions of over 73 %, excluding the sample at 350.49 mbsf when the sand content dropped to zero (Figs. 3, 7). The overall similarity also reveals that the sieved sample record is not strongly biased in those intervals where gypsum crystals formed due to oxidation of pyrite after the sediment cores were opened (as confirmed by sulfite isotope analyses of the gypsum crystals; M. Boettcher, personal communication in 2019) and contributed to the weight of the sand fraction. For the most part of

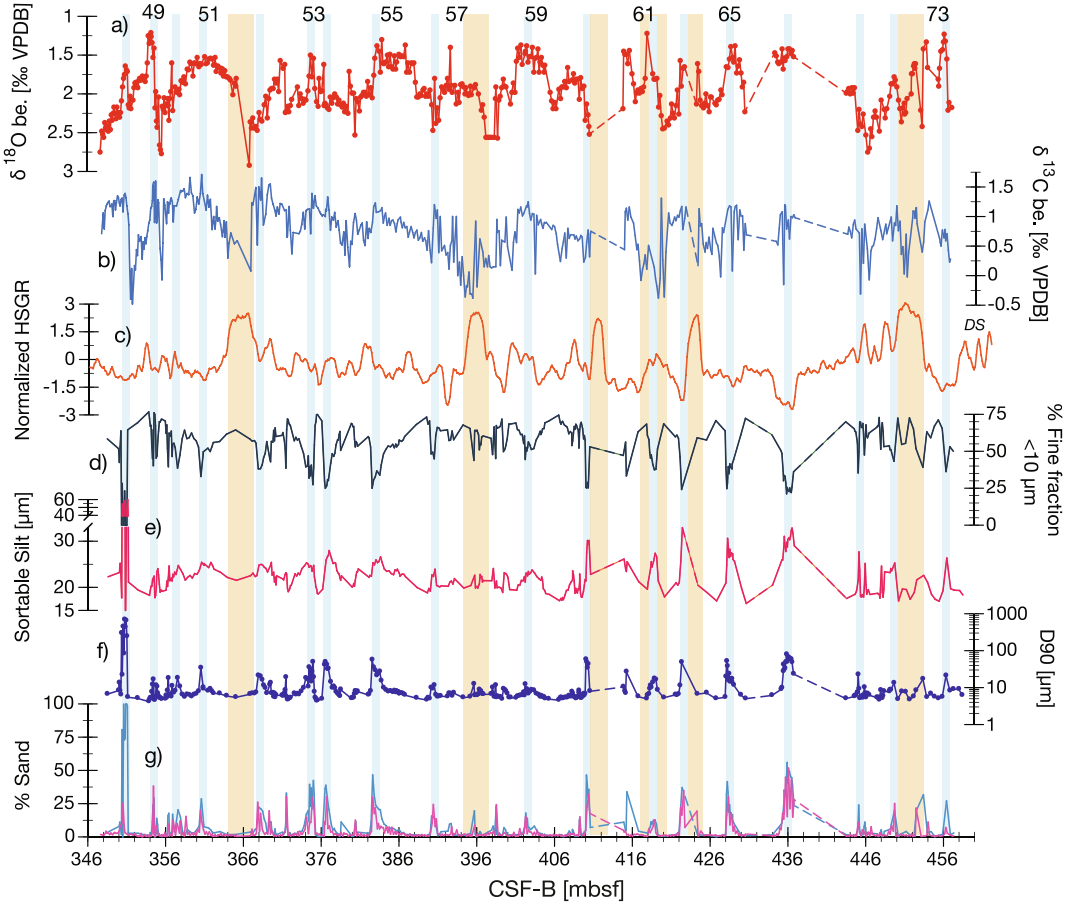

Fig. 7. IODP Site U1387 paleoenvironmental records vs. depth: a) benthic $\delta^{18}O$ record [per mil VPDB] with dots marking respective samples; b) benthic $\delta^{13}C$ data [per mil VPDB]; c) normalized natural gamma ray record (HSGR) from downhole logging (DS = dolostone); d) percentage of clay; e) sortable silt [µm]; f) D90 grain size record [µm]; g) percentage of sand derived from the Malvern Mastersizer analyses (light blue) and from weighing the washed sediment sample (dark magenta). Dashed lines indicate sections with major coring gaps. Orange bars highlight intervals of HSGR maxima and blue bars contourite beds. (For interpretation of the references to colour in this figure legend, the reader is referred to the web version of this article.)

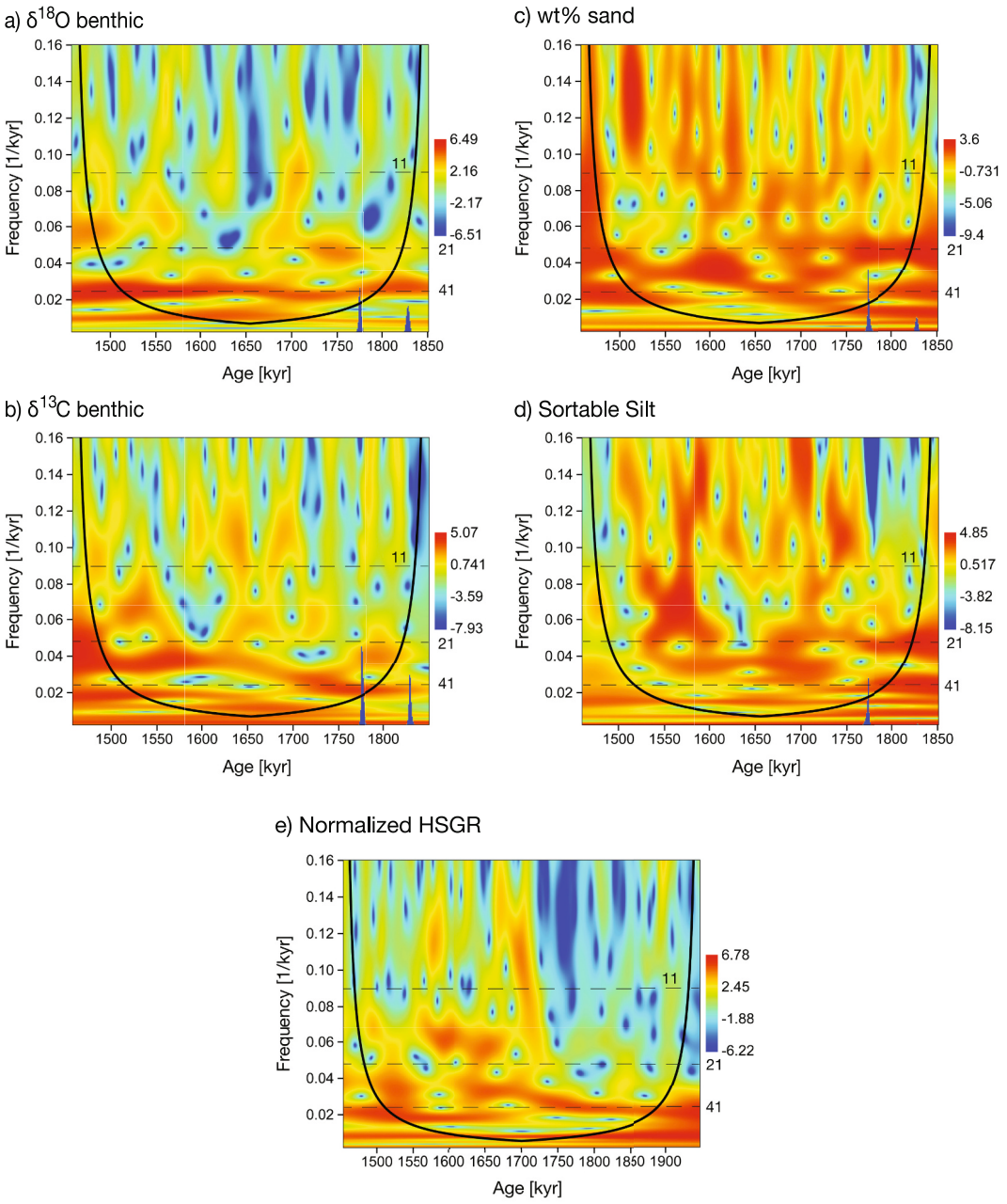

Fig. 8. Wavelet spectral analysis results for benthic $\delta^{18}O$ (a) and $\delta^{13}C$ (b) records as well as wt% sand (from washed samples; c), sortable silt (d), and for the normalized HSGR logging data (e). Whereas spectral analysis for records (a) to (d) was run only for the more continuous interval back to 1.85 Ma, the complete HSGR (back to 1.95 Ma) was analyzed. Dashed horizontal lines and numbers on right indicate obliquity (41 kyr), precession (21 kyr) and semi-precession (11 kyr) bands.

the record, the fine fraction <10 μm and silt dominate the grain size spectrum with sand content only increasing to values above 20 % in the contourite beds (Figs. 3, 7d, f-g). The loss of fine fraction indicates winnowing processes related to bottom current influence in those beds. Thus, the grain size analyses confirm the shipboard core description of silty mud contourites being formed at Site U1387 directly above the youngest dolostone (Expedition 339 Scientists, 2013b) (Fig. 7). As indicated by the D90 values the sand content is mainly within the very fine to fine sand range (Fig. 7f). The sortable silt mean varied mostly between 16 and 30 μm with maxima coinciding with maxima in D90 and wt% sand (Fig. 7). Sortable silt maximum values tend to be higher in the older part of the record (422–438 mbsf). All grain size related records agree with each other, having contemporary maxima, and reveal a clustering of contourite layers between 366 and 386 mbsf, corresponding to MIS 52 to MIS 55 but with a higher density within MIS 53. Unlike the benthic stable isotope records cyclicity in the grain size data on the depth scale is not immediately visible by eye and the timing of the contourite layer emplacement is also not strictly linked to the glacial-interglacial cycles. The normalized HSGR record shows several maxima throughout the interval and one pronounced minimum around 437 mbsf (Fig. 7c). HSGR tends to be higher in core intervals with relatively higher fine fraction <10 μm and silt content (lower sand content) (Lofi et al., 2016), but also lower carbonate content. Despite the overall high fine fraction <10 μm content of the Early Pleistocene sediments at Site U1387, no direct relationship between higher HSGR values and % fine fraction <10 μm is observed (Fig. 7). High HSGR can reflect relatively higher clay content and/or lower sand content. Some HSGR maxima coincide with the pronounced benthic foraminifer $\delta^{13}C$ minima at the onset of MIS 61, MIS 57 and MIS 51. Lower HSGR appears to accompany higher $\overline{SS}$ means marking contourite beds (see MIS 60 to MIS 65 interval

in Fig. 7). So, based on the limited sortable silt and sand content evidence during the HSGR minimum at 422 mbsf, the pronounced HSGR minimum at 437 mbsf might be linked to a contourite bed. The available grain size data would support this, but because the data are from a "floating" section due to the coring gaps, caution should be applied. The dolostones (DS label in Fig. 7c), which mark the Plio-/Pleistocene hiatus (Expedition 339 Scientists, 2013b), are reflected in normalized HSGR as rapid oscillations.

The wt% sand and sortable silt records reveal spectral power within the precession band, but also in sub-orbital scale frequencies (Fig. 8c, d). Power in the shorter periods that are centered around 12–14 kyr (0.08–0.07 kyr^{-1} frequency) and 7–8 kyr (0.14–0.125 kyr^{-1} frequency) and might reflect semi- and quarter-precession periods or combinations of obliquity and precession forcing (Billups and Scheinwald, 2014), is evident especially around 1.72 Ma and between 1.52 and 1.65 Ma. The normalized HSGR spectrum reveals more persistent power in the obliquity band than the precession band, although, similar to the benthic foraminifer $\delta^{13}C$ spectrum, a gradual shift towards the precession band is observed after 1.7 Ma. Comparable to the grain size records, there is also power around the 14 kyr band between 1.56 and 1.67 Ma.

6. Discussion

6.1. Onset of Pleistocene contourite formation at IODP Site U1387

At Site U1387 the dolostones marking the Plio-/Pleistocene hiatus (associated with the Early Quaternary Discontinuity in seismic profiles; Hernández-Molina et al., 2016) occur in sections U1387C-19R-3 and U1387C-19R-4 (DS label in Fig. 7c). The shipboard biostratigraphy indicates a top age close to 2 Ma for the hiatus based on a planktonic foraminifer biostratigraphic event in sample U1387C-19R-3 20–22 cm (456.22 mbsf) (Expedition 339 Scientists, 2013b). The stable isotope chronology for Site U1387 refines the top age now to 1.946 Ma, which marks the recommencement of formation of sandy to muddy contourites at the central section of the Faro Drift in the Pleistocene (Figs. 6, 9). With that age post-hiatus sedimentation started 0.2 Ma earlier at the central Faro Drift than at paleo-moat Site U1386 where hemipelagic sedimentation started within MIS 61 (Fig. 9) (Lebreiro et al., 2015). On the other hand, at the Site U1389, located slightly deeper (644 m) at the Guadalquivir ridge (Fig. 1), the upper MOW branch started to form a contourite drift already during glacial MIS 78 (Kaboth et al., 2017b) (at 2.087 Ma based on the LR04 chronology), thus preceding Site U1387 by about 0.14 Ma (Fig. 9).

Where the isotopic records of Sites U1387 and U1389 overlap and to a lesser extent also Sites U1387 and U1386 (mainly within MIS 58-MIS 59 and MIS 49), they are similar enough that they appear to record the same thermohaline and biogeochemical conditions in the MOW. The very different $\delta^{13}C$ signal between MIS 55-MIS 57 and MIS 49 at Site U1386 might be caused by enhanced admixing of Atlantic water into the MOW recorded in the paleo-moat (Lebreiro et al., 2015) or a reduced MOW influence as proposed for the Middle to Late Pleistocene paleo-moat record (Kaboth et al., 2017a). Furthermore, contribution of reworked benthic foraminifer specimens introduced by gravity-controlled sediment deposition cannot be excluded at Site U1386 (Alonso et al., 2016; García-Gallardo et al., 2017). With MOW temperature and salinity properties apparently being similar at Sites U1387 and U1389 and global sea level not being significantly lower (higher) during the glacial (interglacial) periods of MIS 73 to MIS 78 (Miller et al., 2011;

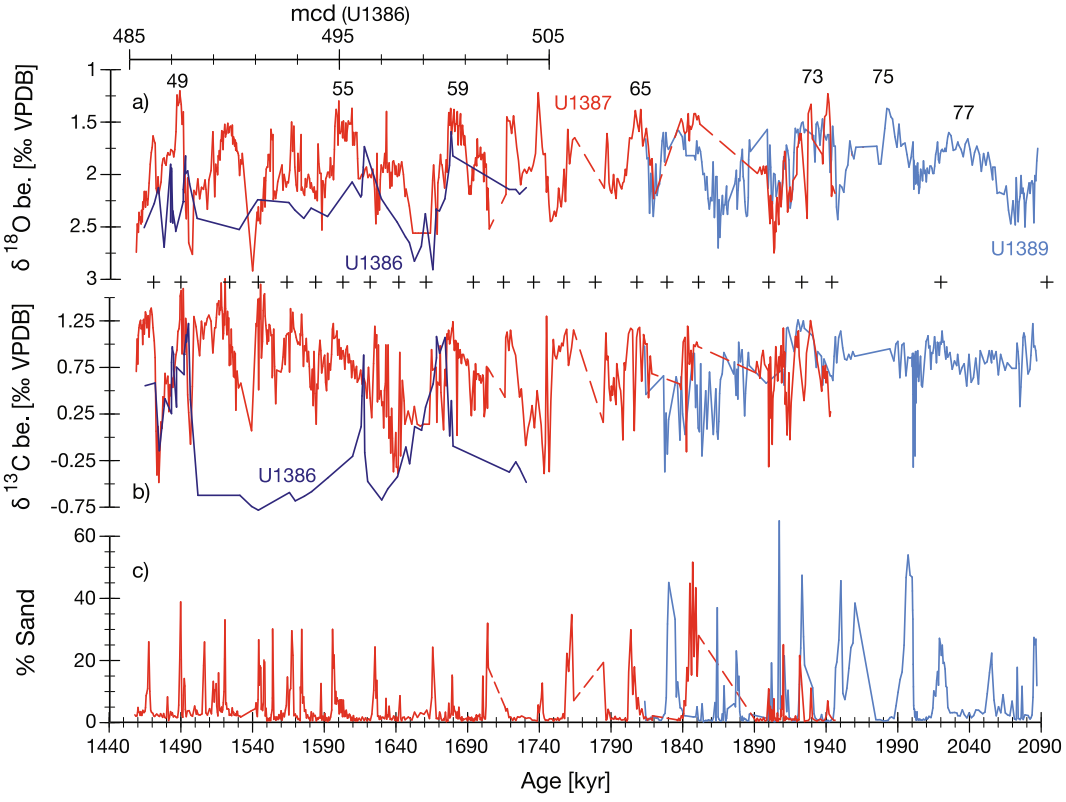

Fig. 9. Comparison of the early Pleistocene benthic $\delta^{18}O$ (panel a) and $\delta^{13}C$ (panel b) records from IODP Sites U1387 (red), U1386 (dark blue) and U1389 (light blue) highlight the agreement between the Gulf of Cádiz MOW records and the age differences for the end of the respective Plio-Pleistocene hiatus (top of younger dolostone). Panel c) shows the weight percentage sand >63 μm (terrigenous and biogenic components) data for Site U1387 (red) and U1389 (light blue). The Site U1389 data (Kaboth et al., 2017b; Kaboth et al., 2017c) is shown on the LR04 related age model generated for this study (Supplementary Fig. S1). The Site U1386 records (Lebreiro et al., 2015), on the other hand, are shown against mcd depth (x-axis on top left in upper panel) and arranged relative to the Site U1387 records for a fit in the better resolved MIS 58-MIS 59 interval, leading to offsets (to the right vs. U1387) for the $\delta^{18}O$ peaks identified as MIS 49 and MIS 55 by Lebreiro et al. (2015). (For interpretation of the references to colour in this figure legend, the reader is referred to the web version of this article.)

Rohling et al., 2014), the cause(s) for the time transgressive resumption of contourite formation by the upper MOW is not understood yet, and needs to be explored further in the future by making use of the new sediment cores collected during IODP Expeditions 397 and 401 (Hodell et al., 2024; Flecker et al., 2025). The resemblance between the two records allows splicing them together for a more complete MOW history in the Gulf of Cádiz during the MIS 65 to MIS 77 interval, also suggesting that the "floating" section within MIS 67-MIS 69 could potentially be 12–14 kyr younger and coincide with the wt% sand maximum dated between 1.828 and 1.836 Ma (late MIS 67) at Site U1389 (Fig. 9c).

Interestingly, the strong upper MOW current during the Plio-/Pleistocene transition that led to the formation of the dolostones in the Gulf of Cádiz sites (Hernández-Molina et al., 2016; Hernández-Molina et al., 2014) also enabled the growth of cold water coral mounds in the Porcupine Seabight (IODP Site U1317; Fig. 1b) (Kano et al., 2007; Raddatz et al., 2014; Sakai et al., 2009; Thierens et al., 2013), which at the Challenger Mound reached maximum growth rates between 2.2 and 2.1 Ma. The mound growth rate rapidly declined shortly after 2.1 Ma, i.e. exactly when MOW contourite sedimentation started at Site U1389 (Kaboth et al., 2017b) (Fig. 9). The re-commencement of contourite formation at the Guadalquivir and Faro Drifts, i.e. at Sites U1389 and U1387, appears to reflect a shift in the water column structure in the Gulf of Cádiz and the eastern North Atlantic, with influence up to the Irish margin. The onset of sedimentation points to a less strong bottom current that allowed for particle accumulation along the upper MOW pathways on the southern Iberian margin. It remains to be seen if that is related to a shift in volume, i.e. more Mediterranean waters feeding into the lower MOW branches instead of the upper branch, and/or a change in the density structure above the upper MOW, i.e. shifts in the salinity and temperature properties of the overlying NACW leading to a lower density gradient between the two water masses. After the re-start, sedimentation was continuous with some variability in the sedimentological properties of the contourite beds (Figs. 3, 7, 9) that would indicate major changes in the strength of the upper MOW current. So, the combined records of Sites U1387 and U1389 provide no insights into why coral mound formation ceased in the Porcupine Seabight between 1.7 and 1 Ma (Kano et al., 2007; Raddatz et al., 2014; Thierens et al., 2013).

6.2. Upper MOW at the central Faro Drift

Despite the relative thin upper MOW layer above the central Faro Drift (Fig. 1b), Early and Middle Pleistocene paleoclimate records for seafloor conditions at Site U1387 have so far always been interpreted as being under continuous MOW influence (Singh et al., 2015; Voelker et al., 2022; Voelker et al., 2015c), even during times of a more sluggish bottom current as previously observed on the Faro Drift during the Late Pleistocene (Lebreiro et al., 2018). In contrast, Middle to Late Pleistocene records from the moat of the Faro Drift, i.e., IODP Site U1386, imply the absence or greatly reduced influence of the upper MOW during MIS 2 to MIS 4 and MIS 6 to MIS 10 (Kaboth et al., 2016; Kaboth et al., 2017a; Moal-Darrigade et al., 2022b). Moreover, studies for periods younger than 1.47 Ma at IODP Sites U1386, U1387 and U1389 (Fig. 1a) established links between NW African monsoon intensification, increased run-off from the Nile river and sapropel formation in the eastern Mediterranean Sea, all related to insolation maxima, and a more sluggish and less well ventilated (low epibenthic foraminifera $\delta^{13}C$ values) MOW in the Gulf of Cádiz (Bahr et al., 2015; Voelker et al., 2015c; Sierro et al., 2020; Voelker et al., 2022). Precipitation intensification was not limited to northern Africa but also affected the Iberian Peninsula increasing run-off from rivers like the Guadalquivir and Guadiana (Fig. 1a) (Bosmans et al., 2015a; Bosmans et al., 2015b). That run-off carried clays like smectite to the Faro Drift (Alonso et al., 2016; Moal-Darrigade et al., 2022a). Higher clay concentration in the sediments increases the natural gamma ray of the formation allowing to link maxima in gamma ray to insolation maxima (Lofi et al., 2016; Sierro et al., 2000). Those causal links are in general confirmed by the Early Pleistocene records from IODP Site U1387, although not all minima in epibenthic $\delta^{13}C$, accompanied by a high fine fraction <10 μm content, are associated with a HSGR maximum (Fig. 7b-d; Fig. 10f, g). Wavelet analysis, furthermore, revealed that HSGR responded more to obliquity than precession forcing (within the age model constraints) between 1.9 and 1.75 Ma (Fig. 8e). Only after 1.75 Ma, precession forcing within the 25–23 kyr band becomes evident in the HSGR and epibenthic $\delta^{13}C$ records (Fig. 8b, e), whereas a dominantly ~21-kyr period signal is observed in wt% sand and sortable silt data (Fig. 8c, d). The different frequency response probably reflects a combination of factors affecting the various proxies, which merits further exploration in the future. The HSGR maximum marking the onset of MIS 51 stands out as both HSGR and epibenthic $\delta^{13}C$ show high amplitude responses, despite occurring during a period marked by low precession and low insolation (Fig. 7; Fig. 10a, f, g).

The sedimentological records, i.e., $\overline{SS}$, D90 and wt% sand (Fig. 7), clearly reveal the persistence of contourite bed formation throughout the Early Pleistocene, conforming with the initial shipboard observations (Expedition 339 Scientists, 2013b). The $\overline{SS}$ data seems to indicate three different phases: 1) a faster MOW (mean speed near 30 μm) in the 1.85–1.7 Ma interval; 2) a slower MOW (low-amplitude mean speed ranging 20–25 μm) between 1.7 and 1.61 Ma; and 3) the cluster of contourites around MIS 53 (25–30 μm mean speed range). An abnormal occurrence is the sandier layer indicated by the Malvern grain size analyses during late MIS 49, which disagrees with the sand weight data from the washed sediment samples (Fig. 7g). This interval corresponds to a highly bioturbated coarse contourite. So, the difference might reflect influences of bioturbation (sandier patches) affecting the smaller sample volume taken for the grain size analyses more strongly than the washed sample series that more likely averages out grain size variability in the highly bioturbated sediment. As already previously observed (e.g., Voelker et al., 2015c; Moal-Darrigade et al., 2022b) and in agreement with the bi-gradational contourite model (Faugères et al., 1984; Stow and Faugères, 2008), the maxima in the wt% sand and D90 mark the sandiest section of a contourite bed, i.e., the period of highest bottom current velocity, whereas the ramping up and tailing in the sortable silt record reflect the gradual increase and decline of current velocity (Fig. 7). The contourite beds were formed during periods with higher epibenthic $\delta^{18}O$ values, i.e., stadials with assumed cooler background climate, and we will explore potential climatic influences and forcing in subchapter 6.3. Formation of contourite beds prevailed in particular during the MIS 55 to MIS 52 interval (1.6–1.5 Ma; Fig. 7; Fig. 11f) in the lead-up to the regime change at 1.5 Ma and synchronous with changes in North Atlantic deep-water circulation (Hodell and Channell, 2016b; Khélifi and Frank, 2014; Lisiecki, 2014). The wavelet analyses revealed that the contourite bed formation occurred at semi- (11 kyr) and quarter-precession (7–8 kyr) periods (Fig. 8c, d). Those periodicities were already previously observed in North Atlantic subtropical gyre surface water records from the Early Pleistocene (Billups and Scheinwald, 2014; Ferretti et al., 2015; Trotta et al., 2025) and the Early Pleistocene MOW at Site U1389 (Kaboth et al., 2017b) and point to a link between lower- to mid-latitudinal insolation forcing and millennial-scale variability in MOW velocity. Following McIntyre and Molfino (1996) and Rutherford and D'Hondt (2000), we assume that modulation in the zonal winds, increased northward heat flux from the tropics to the higher latitudes and their impact on water mass transformation in the North Atlantic's subtropical gyre (e.g., subtropical NACW) played a role.

6.3. Potential drivers for the upper MOW variability and signals

Following Colleoni et al. (2012), we will explore which low-to-mid latitudinal and high-latitudinal processes could be potential drivers for the water mass and sedimentological signals observed at Site U1387.

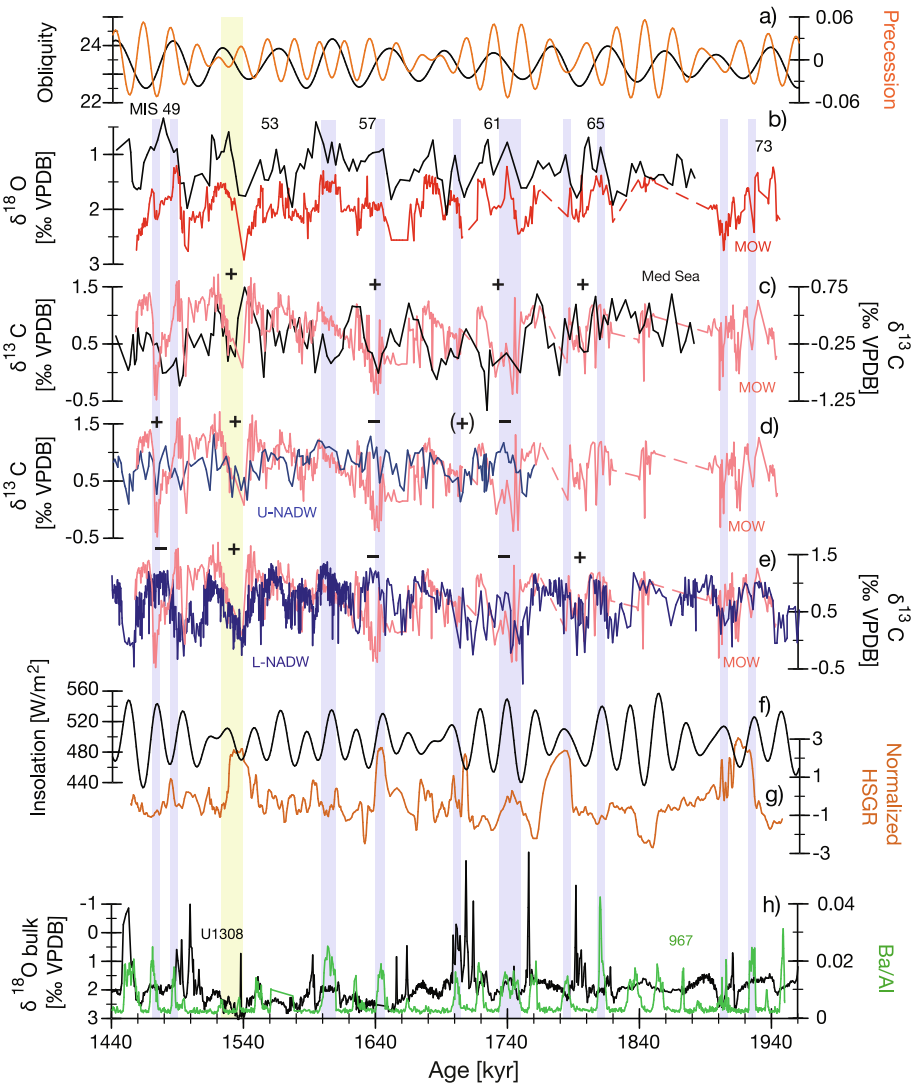

Fig. 10. Water mass influences on the MOW signal at Site U1387: a) Obliquity (black) and precession parameter (orange) (Laskar et al., 2004); b) the IODP Site U1387 benthic $\delta^{18}O$ record (red) in comparison to the *G. bulloides* $\delta^{18}O$ record (black) from ODP Site 975 in the western Mediterranean Sea (Pierre et al., 1999; Pierre et al., 2020) (age model adjusted to LR04); c) to e) the IODP Site U1387 benthic $\delta^{13}C$ data (light red) compared to b) the ODP Site 975 *G. bulloides* $\delta^{13}C$ data (Pierre et al., 1999; Pierre et al., 2020) (black; Y-axis on right), the upper North Atlantic Deep Water (NADW) record from ODP Site 981 (Raymo et al., 2004) (d; blue; converted to LR04 chronology) and lower NADW record from IODP Site U1308 (Hodell and Channell, 2016a; Hodell and Channell, 2016b) (e; dark blue); f) insolation at 37°N on June 21st (Laskar et al., 2004); g) IODP Hole U1387C natural gamma ray record; and h) Detrital carbonate deposition by ice-rafting events at IODP Site U1308 (black) as revealed by lower bulk carbonate $\delta^{18}O$ values (Hodell and Channell, 2016a; Hodell and Channell, 2016b) and sapropel layers in the Eastern Mediterranean Sea as identified by Ba/Al maxima at ODP Site 967 (Grant et al., 2022a; Grant et al., 2022b) (green) with the bars marking some of the sapropel intervals. Plus or minus signs in panels c) to e) indicate periods when the $\delta^{13}C$ records show similar (+) or opposite (−) signals, respectively. Some Marine Isotope Stages (MIS) are indicated in panel b). (For interpretation of the references to colour in this figure legend, the reader is referred to the web version of this article.)

6.3.1. *Mediterranean Sea influences and lower mid-latitude signals*

The MOW in the Gulf of Cádiz is a mixture of the Mediterranean water exiting through the Strait of Gibraltar and the surrounding North Atlantic water masses, in particular the overlying NACW and the underlying AAIW and North Atlantic Deep Water (NADW). The subsurface outflow from the Mediterranean Sea consists of a mixture of Mediterranean intermediate and deep waters (Bryden et al., 1994; Millot, 2014). The intermediate waters are formed in the Levantine basin (Levantine Intermediate Water; LIW) and near Crete (Cretan Intermediate Water), whereas deep convection in the southern regions of the Aegean and Adriatic seas contribute to the Tyrrhenian Dense Water and convection in the Gulf of Lions forms the Western Mediterranean Deep Water (WMDW) (Candela, 2001; Millot et al., 2006; Schroeder et al., 2017). Except for the NADW (Fig. 10d, e), we do not have direct proxy records for the different water masses during our study period. So, we utilize planktonic foraminifer $\delta^{13}C$ records from the Mediterranean Sea (Fig. 10b, c; Supplementary Fig. S2) to infer conditions in Mediterranean Sea surface waters that would be transferred into the intermediate and deep waters and subsequently into the MOW (Kaboth et al., 2017b). In addition, the Ba/Al record of ODP Site 967 in the eastern Mediterranean Sea (Fig. 1b; Fig. 10h) indicates periods when sapropel layers were formed, linked to increased run-off from the Nile river (Grant et al., 2022a; Grant et al., 2022b) and Atlantic moisture (Sierro et al., 2025), whereas its dust record (Fig. 11d) (Larrasoaña et al., 2003) could indicate periods when strong winds might boost ventilation and convection in the Levantine basin and thus formation of LIW.

The comparison between the Mediterranean Sea $\delta^{13}C$ and the Site U1387 epibenthic $\delta^{13}C$ records (Fig. 10c; Supplementary Fig. S2) shows that low ventilation in the surface water and thus (assumed) the LIW and the upper MOW occurred at the same time only during four periods, i.e.,

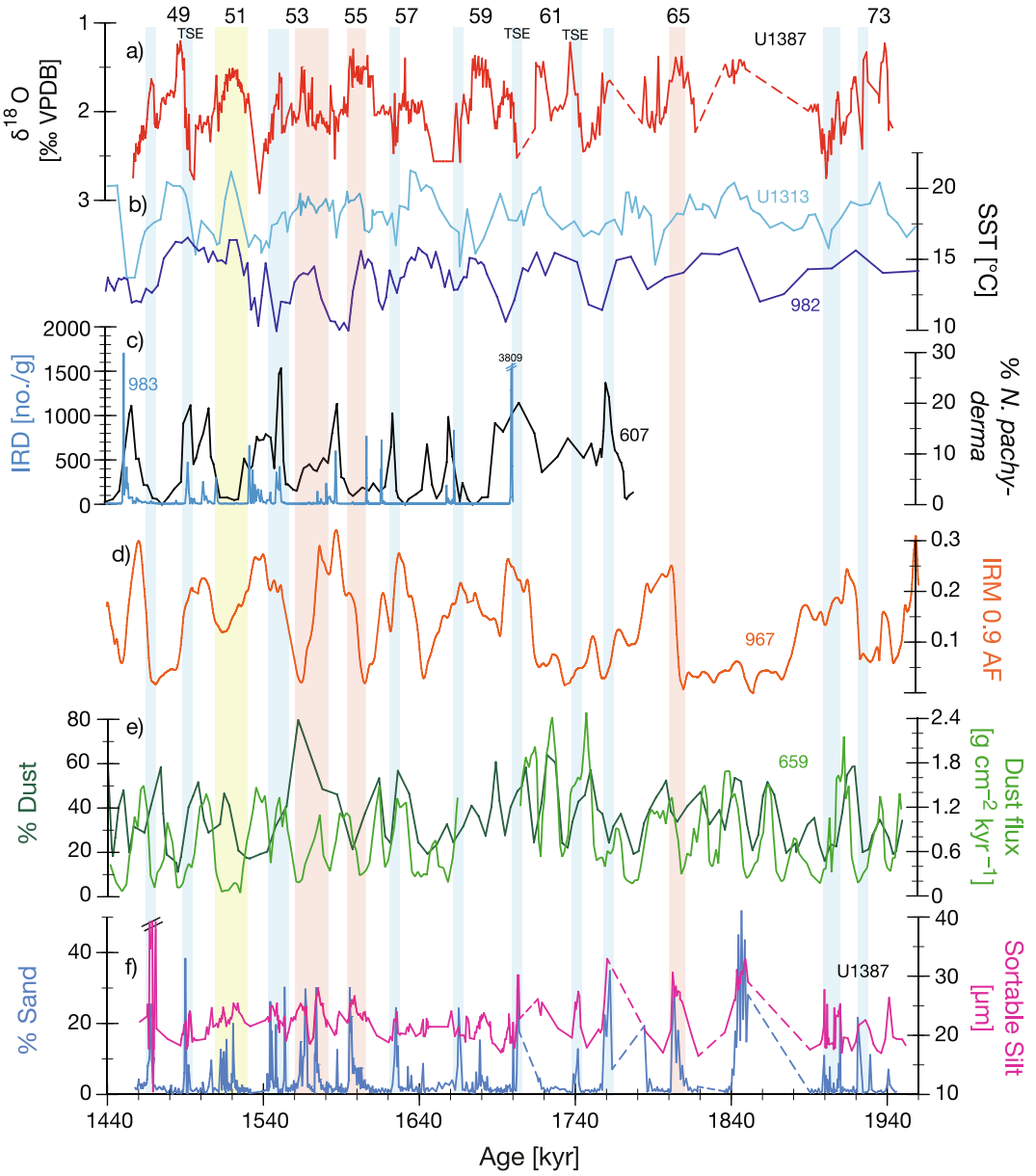

Fig. 11. Low and high latitude influences on the MOW velocity changes: a) the IODP Site U1387 benthic $\delta^{18}O$ record; b) Lipid biomarker derived sea-surface temperature (SST) data for mid-latitudinal IODP Site U1313 (Naafs et al., 2012) and subpolar ODP Site 982 (Lawrence et al., 2009); c) Ice-rafted debris record of subpolar North Atlantic ODP Site 983 (Barker et al., 2022) and the percentage of assumed cold water related planktonic foraminifer *Neogloboquadrina pachyderma* at DSDP Site 607 (same location as U1313) (Ruddiman et al., 1989); d) Saharan dust flux into the eastern Mediterranean Sea at ODP Site 967 (Larrasoaña et al., 2003); e) Saharan dust related records from ODP Site 659 off NW Africa presented as % Dust (dark green; Tiedemann et al., 1994) and as Dust flux (light green; Crocker et al., 2022); f) Sortable silt and weight-% sand records of IODP Site U1387. Orange bars mark contourite bed intervals formed under interglacial climate conditions, blue bars those associated with stadial events and the yellow bar MIS 51. TSE: terminal stadial event; number in a) indicate MIS. (For interpretation of the references to colour in this figure legend, the reader is referred to the web version of this article.)

MIS 64, MIS 61, MIS 57 and MIS 51, whereby only the MIS 61 and MIS 57 intervals coincided with sapropel formation (Fig. 10h). Amplitudes in the $\delta^{13}C$ decline during all four periods were similar at ODP Site 975, located in the Balearic basin (western Mediterranean Sea) (Fig. 1b), within the MedStack (Wang et al., 2010) (Supplementary Fig. S2 upper panel) and the Site U1387 MOW record, whereas they diverge from the ODP Site 967 record in the Levantine Sea (eastern Mediterranean Sea) (Supplementary Fig. S2 lower panel). We assume that during all those periods poorly ventilated LIW contributed to the MOW at Site U1387, even if Lebreiro et al. (2015) indicate a strong Atlantic water presence in the moat of the Faro Drift (IODP Site U1386) during the interglacial periods between MIS 39 and MIS 59. The water depth of Site U1387 is too shallow for any AAIW influence, so that we exclude AAIW as source for the low $\delta^{13}C$ waters, conforming with Voelker et al. (2015c). Because sapropel formation occurred mainly during interglacial periods, deep-water formation in the North Atlantic should be active and produce well-ventilated deep (and central) waters. This is in general confirmed by the upper and lower NADW records from ODP Site 981 and IODP Site U1308 (Fig. 10d, e). Only during glacial MIS 64 and the stadial event during MIS 49 lesser ventilated waters from the upper water column in the North Atlantic might have contributed to the signal at Site U1387 (Fig. 10d). However, MIS 51 (1.51–1.53 Ma) stands out as an enigmatic period as ventilation is poor across the complete water column, i.e., from the surface waters all the way down into the lower NADW depth range at IODP Site U1308 and contemporary in the Mediterranean Sea and the North Atlantic Ocean (Fig. 10c-e). The poor ventilation started already

in MIS 52 (mostly lacking in U1387 because of the core transition) and lasted 8 kyr into the interglacial (until 1.522 Ma), whereby the low $\delta^{13}C$ values at Site U1308 would point to the presence of southern sourced waters (Antarctic Bottom Water levels) and thus a much-reduced Atlantic meridional overturning circulation. The strong perturbation in the ventilation of the North Atlantic under interglacial conditions and consequently in the carbon cycle merits further exploration in the future, because those signals are not clear. Sea-ice changes in the Nordic Seas as proposed by Raymo et al. (2004) to explain Early Pleistocene glacial lower $\delta^{13}C$ values in the intermediate depths (1150–2300 m) should normally not apply for an interglacial period and the Site U1308 bulk carbonate $\delta^{18}O$ record (Fig. 10h) shows only a minor event at the onset of MIS 52, although further to the north at Site 983 persistent ice-rafted debris deposition was recorded (Fig. 11c) (Barker et al., 2022).

Given the age model constraints and differences in temporal resolution between the ODP Site 967 dust record (Larrasoaña et al., 2003) and the Site U1387 benthic $\delta^{13}C$ and contourite bed records, causal links need to be inferred cautiously. The contourite beds during MIS 65 and the MIS 57 – MIS 55 interval were formed under warm, interglacial climate conditions (Fig. 11b), in contrast to many of the other contourite beds (see 6.3.2; Voelker et al., 2015c; Voelker et al., 2022). Therefore, velocity increases in the MOW were not linked to a density gradient between less saline, cooler North Atlantic surface waters and the saline Mediterranean waters (Rogerson et al., 2012a; Rogerson et al., 2012b). In agreement with Late to Early Pleistocene observations (Lebreiro et al., 2015; Voelker et al., 2015c; Kaboth et al., 2016; Kaboth et al., 2017b; Moal-Darrigade et al., 2022b; Voelker et al., 2022), the upper MOW was well ventilated during periods of contourite bed formation (Fig. 7) and increased windiness in the Eastern Mediterranean Sea (more dust at Site 967; Fig. 11d) appears to have produced a well-ventilated LIW (as reflected in the generally high planktonic $\delta^{13}C$ data at Site 967 and in the MedStack; Supplementary Fig. S2). Well-ventilated LIW and WMDW were observed during windier, although colder, climate periods of the last glacial cycle (Moreno et al., 2005; Cacho et al., 2006; Frigola et al., 2008; Toucanne et al., 2012), supporting our assumption that the same occurred during the Early Pleistocene and contributed to the MOW signal at Site U1387. As windier conditions were also recorded off NW Africa (ODP Site 659; Fig. 11e) (Tiedemann et al., 1994; Crocker et al., 2022), enhanced atmospheric circulation over all of northern Africa that could have increased evaporation can be inferred, thereby increasing salinity and subsequently density in the Mediterranean intermediate and deep waters that fed into the MOW. Thus, those interglacial contourite beds appear to be linked to atmospheric conditions in the Mediterranean Sea region. The exception to the rule might be again MIS 51 when neither contemporary increased dust (wind; giving more weight to the higher resolution record of Crocker et al. (2022)) nor cooler North Atlantic surface waters (see 6.3.2) were observed (Fig. 11).

6.3.2. *High latitude influences*

The majority of the Pleistocene contourite beds were formed during stadials (or Greenland stadials during MIS 2 – MIS 5) including the terminal stadial events occurring during deglaciation (Voelker et al., 2006; Voelker et al., 2015c; Sierro et al., 2020; Moal-Darrigade et al., 2022b; Voelker et al., 2022). Rogerson et al. (2012a, 2012b) explained the increased flow velocity during the colder periods with the increased density gradient between the less saline (and thus less dense) North Atlantic surface waters in the Gulf of Cádiz and the saline (dense) Mediterranean waters entering the Gulf of Cádiz. The colder, less saline surface waters are linked to ice-sheet disintegration and ice-rafting in the North Atlantic and the related shift in oceanographic fronts in the North Atlantic (e.g., Voelker et al., 2006; Voelker et al., 2022). The same concepts should apply to the Early Pleistocene contourite beds not occurring under interglacial conditions. The Site U1387 records reveal contourite beds related to the terminal stadial events of MIS 50, MIS 60 and MIS 62, which were all associated with ice-rafting and cooler sea-surface temperatures in the North Atlantic (Fig. 10h; Fig. 11b, c). The majority of stadial related contourite beds were, however, formed as part of the millennial-scale climate variability occurring during the transition from interglacial to full glacial conditions, namely during late MIS 51, MIS 53, MIS 57, MIS 59, and probably MIS 63 and the transition from MIS 73 into MIS 72. Most of those periods were characterized by cooler surface water conditions (within temporal resolution and age model constrains) in the North Atlantic (Fig. 11b, c), but not necessarily ice-rafting in the mid-latitudinal North Atlantic (e.g., MIS 73, MIS 57; Fig. 10h; Fig. 11c). This probably reflects the smaller Laurentide ice sheet (Bintanja and van de Wal, 2008) and reduced glacial erosion (sedimentation) rates from the Scandinavian ice sheet as recorded along the Norwegian margin and in the North Sea during that time (Lien et al., 2022).

7. Conclusions

The millennial-scale time series of IODP Site U1387, although hampered by coring related sediment gaps in the older sequence, provide insights into the history of the upper MOW core above the central Faro Drift. Nannofossil biostratigraphic data and paleomagnetic and $\delta^{18}O$ stratigraphy provide a rigorous stratigraphic framework for the time series. Early Pleistocene sedimentation of sandy to muddy contourites restarted at 1.946 Ma, i.e., within Marine Isotope Stage (MIS) 74, and thus slightly younger than at IODP Site U1389. The sortable silt and sand percentage records clearly highlight the contourite beds, whose formation was strongly influenced by precession-driven climate forcing, including both semi- and quarter-precession cycles. Most of the contourite beds developed during stadial (colder) climate periods, including the terminal stadials of MIS 50, MIS 60 and MIS 62, consistent with earlier findings from the Early to Late Pleistocene in the Gulf of Cádiz and along the southwestern Portuguese margin. Their formation is therefore related to the high latitude processes associated with ice sheet instabilities and their impact on North Atlantic thermohaline circulation. Contourite beds within MIS 53, MIS 55 and MIS 65, developed under interglacial conditions and their formation appears to be linked to the prevailing atmospheric (windy) conditions over North Africa, i.e., low- to mid-latitudinal processes. Conforming with the observations of Lofi et al. (2016), maxima in the natural gamma ray occurred during periods with high fine fraction <10 μm content and low ventilation in the upper MOW core, related to insolation maxima. Poor ventilation in the upper MOW was linked to reduced ventilation in Mediterranean Sea surface waters, although lesser ventilated North Atlantic waters might sometimes also have contributed to the $\delta^{13}C$ signals at Site U1387. One such case would be MIS 51, when poor ventilation was observed throughout the water column from the surface to the lower NADW range and contemporary in the Mediterranean Sea and the North Atlantic. As those unique conditions lasted 8 kyr into the interglacial, MIS 51 presents a peculiar case that merits further exploration in the future.

CRediT authorship contribution statement

Antje H.L. Voelker: Writing – review & editing, Writing – original draft, Visualization, Validation, Supervision, Project administration, Investigation, Funding acquisition, Formal analysis, Data curation, Conceptualization. **Emanuelle Ducassou:** Writing – review & editing, Visualization, Validation, Project administration, Investigation, Funding acquisition, Data curation, Conceptualization. **Barbara Balestra:** Writing – review & editing, Validation, Investigation, Data curation, Conceptualization. **Jose Abel Flores:** Writing – review & editing, Validation, Investigation, Conceptualization. **Gary D. Acton:** Writing – review & editing, Visualization, Validation, Project administration, Methodology, Investigation, Funding acquisition, Formal analysis, Data curation, Conceptualization. **Carl Richter:** Writing – review & editing, Validation, Project administration, Investigation, Funding acquisition, Conceptualization. **Chuang Xuan:** Writing – review & editing, Validation, Investigation. **Johanna Lofi:** Writing – review & editing,

Validation, Investigation. **Ana Alberto:** Investigation. **Henning Kuhnert:** Writing – review & editing, Validation, Investigation. **Carlos A. Alvarez Zarikian:** Writing – review & editing, Resources.

Declaration of competing interest

The authors declare the following financial interests/personal relationships which may be considered as potential competing interests:

Given her role as editorial board member, Antje Voelker had no involvement in the peer review of this article and had no access to information regarding its peer review. Full responsibility for the editorial process for this article was delegated to another journal editor. If there are other authors, they declare that they have no known competing financial interests or personal relationships that could have appeared to influence the work reported in this paper.

Acknowledgements

The samples for this study were provided by the Integrated Ocean Drilling Program (2003−2013) and we thank the Bremen Core Repository and its staff for sampling the sections. The stable isotope analyses and related laboratory work were funded by Fundação para a Ciência e a Tecnologia (FCT) project MOWCADYN (PTDC/MAR-PRO/3761/2012). Scanning electron microscope work was made possible through the EMSO-PT infrastructure project with grant number POCI-01-0145-FEDER-022157. A. Voelker received additional funding from FCT through her *Investigador FCT* grant (IF/01500/2014) and CCMAR/CIMAR LA contracts UID/04326/2025, UID/PRR/04326/2025 and LA/P/0101/2020 (DOI:10.54499/LA/P/0101/2020). She also warmly thanks Joachim Schönfeld (Geomar, Kiel), Ann Holbourn, Wolfgang Kuhnt (both IfG, Univ. Kiel) and Tom Dignes (East Falmouth, USA) for their help in benthic foraminifer species identification and Michael Boettcher (IO, Warnemuende) for the isotope analyses in the gypsum crystals, following a suggestion from Geert de Lange (Uni. Utrecht). C. Veiga-Pires (Univ. Algarve) provided laboratory space and support to A. Alberto. G. Acton and C. Richter were funded by the National Science Foundation (NSF) grant OCE-1334163 and by the U.S. Science Support Program (USSSP), which is funded by NSF OCE-1450528. C. Alvarez Zarikian was also funded by USSSP. B. Balestra was also supported by a PEA IODP award. Grain size analyses for E. Ducassou were funded by the IODP-France support program. Funding for Jose-Abel Flores through the projects PID2021-128322NB-I00 and PID2024-158309NB-I00 from Ministerio de Ciencia, Innovación y Universidades of Spain are also acknowledged. We also thank the two reviewers for their positive feedback that helped to improve the manuscript.

Appendix A. Supplementary data

Supplementary data to this article can be found online at https://doi.org/10.1016/j.margeo.2025.107697.

Data availability

The data from the discrete samples analyses have been archived at the World Data Center PANGAEA (Felden et al., 2023) and the data bundle is accessible via https://doi.org/10.1594/PANGAEA.987448. The downhole logging data for normalized HSGR is available from IODP at https://mlp.ldeo.columbia.edu/data/.

References

Acton, G., 2011. ZPLOTIT Software Users' Guide Version, version 2011–01, Book ZPLOTIT Software Users' Guide Version, version 2011–01. http://paleomag.ucdavis.edu/Software/Zplotit/ZPLOTIT-Users-Guide-v2011-01.pdf.

Alonso, B., Ercilla, G., Casas, D., Stow, D.A.V., Rodríguez-Tovar, F.J., Dorador, J., Hernández-Molina, F.-J., 2016. Contourite vs gravity-flow deposits of the Pleistocene Faro Drift (Gulf of Cadiz): sedimentological and mineralogical approaches. Mar. Geol. 377, 77–94. https://doi.org/10.1016/j.margeo.2015.12.016.

Ambar, I., Howe, M.R., 1979. Observations of the Mediterranean outflow: 1. Mixing in the Mediterranean outflow. Deep Sea Res. A 26, 535–554.

Anthonissen, D.E., Ogg, J.G., 2012. Appendix 3 - Cenozoic and Cretaceous biochronology of planktonic foraminifera and calcareous nannofossils. In: Gradstein, F.M., Ogg, J. G., Schmitz, M., Ogg, G. (Eds.), The Geologic Time Scale 2012. Elsevier, pp. 1083–1126.

Aubry, M.-P., Couvering, J.A.V., Christie-Blick, N., Landing, E., Pratt, B.R., Owen, D.E., Ferrusquía-Villafranca, I., 2009. Terminology of geological time: establishment of a community standard. Stratigraphy 6, 100–105.

Bahr, A., Kaboth, S., Jiménez-Espejo, F.J., Sierro, F.J., Voelker, A.H.L., Lourens, L., Röhl, U., Reichart, G.J., Escutia, C., Hernández-Molina, F.J., Pross, J., Friedrich, O., 2015. Persistent monsoonal forcing of Mediterranean Outflow Water dynamics during the late Pleistocene. Geology 43, 951–954. https://doi.org/10.1130/G37013.1.

Balestra, B., Voelker, A., Flores, J.-A., 2019. Data report: early Pleistocene calcareous nannofossils, IODP Expedition 339, Site U1387. In: Stow, D.A.V., Hernández-Molina, F.J., Alvarez Zarikian, C.A., the Expedition 339 Scientists (Eds.), Proceedings of the Integrated Ocean Drilling Program, 339. Integrated Ocean Drilling Program Management International, Inc, Tokyo, pp. 1–5. https://doi.org/10.2204/iodp.proc.339.205.2019.

Baringer, M.O., Price, J.F., 1997. Mixing and spreading of the Mediterranean outflow. J. Phys. Oceanogr. 27, 1654–1677.

Barker, S., Starr, A., van der Lubbe, J., Doughty, A., Knorr, G., Conn, S., Lordsmith, S., Owen, L., Nederbragt, A., Hemming, S., Hall, I., Levay, L., Berke, M.A., Brentegani, L., Caley, T., Cartagena-Sierra, A., Charles, C.D., Coenen, J.J., Crespin, J. G., Franzese, A.M., Gruetzner, J., Han, X., Hines, S.K.V., Jimenez Espejo, F.J., Just, J., Koutsodendris, A., Kubota, K., Lathika, N., Norris, R.D., Periera dos Santos, T., Robinson, R., Rolison, J.M., Simon, M.H., Tangunan, D., Yamane, M., Zhang, H., 2022. Persistent influence of precession on northern ice sheet variability since the early Pleistocene. Science 376, 961–967. https://doi.org/10.1126/science.abm4033.

Billups, K., Scheinwald, A., 2014. Origin of millennial-scale climate signals in the subtropical North Atlantic. Paleoceanography 29, 2014PA002641. https://doi.org/10.1002/2014PA002641.

Bintanja, R., van de Wal, R.S.W., 2008. North American ice-sheet dynamics and the onset of 100,000-year glacial cycles. Nature 454, 869–872.

Bosmans, J.H.C., Drijfhout, S.S., Tuenter, E., Hilgen, F.J., Lourens, L.J., 2015a. Response of the North African summer monsoon to precession and obliquity forcings in the EC-Earth GCM. Climate Dynam. 44, 279–297. https://doi.org/10.1007/s00382-014-2260-z.

Bosmans, J.H.C., Drijfhout, S.S., Tuenter, E., Hilgen, F.J., Lourens, L.J., Rohling, E.J., 2015b. Precession and obliquity forcing of the freshwater budget over the Mediterranean. Quat. Sci. Rev. 123, 16–30. https://doi.org/10.1016/j.quascirev.2015.06.008.

Bryden, H.L., Candela, J., Kinder, T.H., 1994. Exchange through the Strait of Gibraltar. Prog. Oceanogr. 33, 201–248.

Cabeçadas, G., Brogueira, M.J., Goncalves, C., 2002. The chemistry of Mediterranean outflow and its interactions with surrounding waters. Deep-Sea Res. II Top. Stud. Oceanogr. 49, 4263–4270.

Cabeçadas, G., Brogueira, M.J., Gonçalves, C., 2003. Intermediate water masses off south-southwest Portugal: chemical tracers. J. Mar. Res. 61, 539–552.

Cabeçadas, G., José Brogueira, M., Gelena Cavaco, M., Gonçalves, C., 2010. Chemical signature of intermediate water masses along western Portuguese margin. J. Oceanogr. 66, 201–210. https://doi.org/10.1007/s10872-010-0018-8.

Cacho, I., Shackleton, N., Elderfield, H., Sierro, F.J., Grimalt, J.O., 2006. Glacial rapid variability in deep-water temperature and δ18O from the Western Mediterranean Sea. Quat. Sci. Rev. 25, 3294–3311. https://doi.org/10.1016/j.quascirev.2006.10.004.

Candela, J., 2001. Mediterranean water and global circulation. In: Siedler, G., Church, J., Gould, J. (Eds.), Ocean Circulation and Climate – Observing and Modelling the Global Ocean. Academic Press, San Diego, London, pp. 419–429.

Castañeda, I.S., Schouten, S., Pätzold, J., Lucassen, F., Kasemann, S., Kuhlmann, H., Schefuß, E., 2016. Hydroclimate variability in the Nile River Basin during the past 28,000 years. Earth Planet. Sci. Lett. 438, 47–56. https://doi.org/10.1016/j.epsl.2015.12.014.

Channell, J.E.T., Hodell, D.A., Curtis, J.H., 2016. Relative paleointensity (RPI) and oxygen isotope stratigraphy at IODP Site U1308: North Atlantic RPI stack for 1.2–2.2 Ma (NARPI-2200) and age of the Olduvai Subchron. Quat. Sci. Rev. 131 (Part A), 1–19. https://doi.org/10.1016/j.quascirev.2015.10.011.

Channell, J.E.T., Singer, B.S., Jicha, B.R., 2020. Timing of Quaternary geomagnetic reversals and excursions in volcanic and sedimentary archives. Quat. Sci. Rev. 228, 106114. https://doi.org/10.1016/j.quascirev.2019.106114.

Clark, P.U., Shakun, J.D., Rosenthal, Y., Köhler, P., Bartlein, P.J., 2024. Global and regional temperature change over the past 4.5 million years. Science 383, 884–890. https://doi.org/10.1126/science.adi1908.

Colleoni, F., Masina, S., Negri, A., Marzocchi, A., 2012. Plio–Pleistocene high–low latitude climate interplay: a Mediterranean point of view. Earth Planet. Sci. Lett. 319-320, 35–44. https://doi.org/10.1016/j.epsl.2011.12.020.

Crocker, A.J., Naafs, B.D.A., Westerhold, T., James, R.H., Cooper, M.J., Röhl, U., Pancost, R.D., Xuan, C., Osborne, C.P., Beerling, D.J., Wilson, P.A., 2022. Astronomically controlled aridity in the Sahara since at least 11 million years ago. Nat. Geosci. 15, 671–676. https://doi.org/10.1038/s41561-022-00990-7.

Da, J., Zhang, Y.G., Li, G., Meng, X., Ji, J., 2019. Low CO2 levels of the entire Pleistocene epoch. Nat. Commun. 10, 4342. https://doi.org/10.1038/s41467-019-12357-5.

Dyez, K.A., Hönisch, B., Schmidt, G.A., 2018. Early Pleistocene obliquity-scale pCO2 variability at ~1.5 million years ago. Paleoceanogr. Paleoclimatol. 33, 1270–1291. https://doi.org/10.1029/2018PA003349.

Emeis, K.-C., Sakamoto, T., Wehausen, R., Brumsack, H.-J., 2000. The sapropel record of the eastern Mediterranean Sea – results of Ocean Drilling Program Leg 160. Palaeogeogr. Palaeoclimatol. Palaeoecol. 158, 371–395. https://doi.org/10.1016/S0031-0182(00)00059-6.

Emeis, K.-C., Schulz, H., Struck, U., Rossignol-Strick, M., Erlenkeuser, H., Howell, M.W., Kroon, D., Mackensen, A., Ishizuka, S., Oba, T., Sakamoto, T., Koizumi, I., 2003. Eastern Mediterranean surface water temperatures and $\delta^{18}O$ composition during deposition of sapropels in the late Quaternary. Paleoceanography 18, 1005. https://doi.org/10.1029/2000PA000617.

Methods. In: Expedition 339 Scientists, Stow, D.A.V., Hernández-Molina, F.J., Alvarez Zarikian, C.A., the Expedition 339 Scientists (Eds.), 2013a. Proceedings IODP Exp. 339 - Mediterranean Outflow. Integrated Ocean Drilling Program Management International, Inc., Tokyo https://doi.org/10.2204/iodp.proc.339.102.2013.

Site U1387. In: Expedition 339 Scientists, Stow, D.A.V., Hernández-Molina, F.J., Alvarez Zarikian, C.A., the Expedition 339 Scientists (Eds.), 2013b. Proceedings IODP Exp. 339 - Mediterranean Outflow. Integrated Ocean Drilling Program Management International, Inc, Tokyo. https://doi.org/10.2204/iodp.proc.339.105.2013.

Faugères, J., Gonthier, E., Stow, D., 1984. Contourite drift molded by deep Mediterranean Outflow. Geology 12, 296–300.

Felden, J., Möller, L., Schindler, U., Huber, R., Schumacher, S., Koppe, R., Diepenbroek, M., Glöckner, F., 2023. PANGAEA – data publisher for earth & environmental science. Sci. Data 10, 347. https://doi.org/10.1038/s41597-023-02269-x.

Ferretti, P., Crowhurst, S.J., Naafs, B.D.A., Barbante, C., 2015. The Marine Isotope Stage 19 in the mid-latitude North Atlantic Ocean: astronomical signature and intra-interglacial variability. Quat. Sci. Rev. 108, 95–110. https://doi.org/10.1016/j.quascirev.2014.10.024.

Flecker, R., Ducassou, E., Williams, T., and the Expedition 401 Scientists, 2025. Mediterranean–Atlantic Gateway Exchange. Proceedings of the International Ocean Discovery Program, 401, International Ocean Discovery Program, College Station, TX; doi:10.14379/iodp.proc.401.2025.

Flores, J.A., Sierro, F.J., 1997. Revised technique for calculation of calcareous nannofossil accumulation rates. Micropaleontology 43, 321–324.

Foster, G., 1996. Wavelets for period analysis of unevenly sampled time series. Astron. J. 112, 1709–1729.

Frigola, J., Moreno, A., Cacho, I., Canals, M., Sierro, F.J., Flores, J.A., Grimalt, J.O., 2008. Evidence of abrupt changes in Western Mediterranean Deep Water circulation during the last 50 kyr: a high-resolution marine record from the Balearic Sea. Quat. Int. 181, 88–104. https://doi.org/10.1016/j.quaint.2007.06.016.

García-Gallardo, Á., Grunert, P., Voelker, A.H.L., Mendes, I., Piller, W.E., 2017. Re-evaluation of the "elevated epifauna" as indicator of Mediterranean Outflow Water in the Gulf of Cadiz using stable isotopes (δ13C, δ18O). Global Planet. Change 155, 78–97. https://doi.org/10.1016/j.gloplacha.2017.06.005.

Grant, K.M., Amarathunga, U., Amies, J., Hu, P., Qian, Y., Penny, T., Rodriguez-Sanz, L., Zhao, X., Heslop, D., Liebrand, D., Hennekam, R., Westerhold, T., Gilmore, S., Lourens, L.J., Roberts, A., Rohling, E.J., 2022a. Plio-Pleistocene scanning XRF, stable isotope, and environmental magnetic data from ODP Site 967. PANGAEA. https://doi.org/10.1594/PANGAEA.939929.

Grant, K.M., Amarathunga, U., Amies, J.D., Hu, P., Qian, Y., Penny, T., Rodriguez-Sanz, L., Zhao, X., Heslop, D., Liebrand, D., Hennekam, R., Westerhold, T., Gilmore, S., Lourens, L.J., Roberts, A.P., Rohling, E.J., 2022b. Organic carbon burial in Mediterranean sapropels intensified during Green Sahara Periods since 3.2 Myr ago. Commun. Earth Environ. 3. https://doi.org/10.1038/s43247-021-00339-9.

Hammer, Ø., Harper, D.A.T., Ryan, P.D., 2001. PAST: paleontological statistics software package for education and data analysis. Palaeontol. Electron. 4, 1–9.

Head, M.J., Gibbard, P.L., 2015. Early–Middle Pleistocene transitions: linking terrestrial and marine realms. Quat. Int. 389, 7–46. https://doi.org/10.1016/j.quaint.2015.09.042.

Hernández-Molina, F.J., Stow, D.A.V., Alvarez-Zarikian, C.A., Acton, G., Bahr, A., Balestra, B., Ducassou, E., Flood, R., Flores, J.-A., Furota, S., Grunert, P., Hodell, D., Jimenez-Espejo, F., Kim, J.K., Krissek, L., Kuroda, J., Li, B., Llave, E., Lofi, J., Lourens, L., Miller, M., Nanayama, F., Nishida, N., Richter, C., Roque, C., Pereira, H., Sanchez Goñi, M.F., Sierro, F.J., Singh, A.D., Sloss, C., Takashimizu, Y., Tzanova, A., Voelker, A., Williams, T., Xuan, C., 2014. Onset of Mediterranean outflow into the North Atlantic. Science 344, 1244–1250. https://doi.org/10.1126/science.1251306.

Hernández-Molina, F.J., Sierro, F.J., Llave, E., Roque, C., Stow, D.A.V., Williams, T., Lofi, J., Van der Schee, M., Arnáiz, A., Ledesma, S., Rosales, C., Rodríguez-Tovar, F.J., Pardo-Igúzquiza, E., Brackenridge, R.E., 2016. Evolution of the gulf of Cadiz margin and southwest Portugal contourite depositional system: tectonic, sedimentary and paleoceanographic implications from IODP expedition 339. Mar. Geol. 377, 7–39. https://doi.org/10.1016/j.margeo.2015.09.013.

Hilgen, F.J., Lourens, L.J., Berger, A., Loutre, M.F., 1993. Evaluation of the astronomically calibrated time-scale for the Late Pliocene and Earliest Pleistocene. Paleoceanography 8, 549–565.

Hines, S.K.V., Charles, C.D., Starr, A., Goldstein, S.L., Hemming, S.R., Hall, I.R., Lathika, N., Passacantando, M., Bolge, L., 2024. Revisiting the mid-Pleistocene transition ocean circulation crisis. Science 386, 681–686. https://doi.org/10.1126/science.adn4154.

Hodell, D.A., Channell, J.E.T., 2016a. Foraminiferal stable isotopes and physical properties from North Atlantic sediment cores for the past 3.2 million years. PANGAEA. https://doi.org/10.1594/PANGAEA.871937.

Hodell, D.A., Channell, J.E.T., 2016b. Mode transitions in Northern Hemisphere glaciation: co-evolution of millennial and orbital variability in Quaternary climate. Clim. Past 12, 1805–1828. https://doi.org/10.5194/cp-12-1805-2016.

Hodell, D.A., Abrantes, F., Alvarez Zarikian, C.A., the Expedition Scientists, 2024. Iberian Margin Paleoclimate. Proceedings of the International Ocean Discovery Program, 397. International Ocean Discovery Program, College Station, TX. https://doi.org/10.14379/iodp.proc.397.2023.

Hönisch, B., Hemming, N.G., Archer, D., Siddall, M., McManus, J.F., 2009. Atmospheric carbon dioxide concentration across the mid-Pleistocene transition. Science 324, 1551–1554. https://doi.org/10.1126/science.1171477.

Huybers, P., 2007. Glacial variability over the last two million years: an extended depth-derived agemodel, continuous obliquity pacing, and the Pleistocene progression. Quat. Sci. Rev. 26, 37–55.

Kaboth, S., Bahr, A., Reichart, G.-J., Jacobs, B., Lourens, L.J., 2016. New insights into upper MOW variability over the last 150 kyr from IODP 339 Site U1386 in the Gulf of Cadiz. Mar. Geol. 377, 136–145. https://doi.org/10.1016/j.margeo.2015.08.014.

Kaboth, S., Boer, B., Bahr, A., Zeeden, C., Lourens, L.J., 2017a. Mediterranean outflow water dynamics during the past ~570 kyr: regional and global implications. Paleoceanography 32, 634–647. https://doi.org/10.1002/2016PA003063.

Kaboth, S., Grunert, P., Lourens, L., 2017b. Mediterranean outflow water variability during the Early Pleistocene. Clim. Past 13, 1023–1035. https://doi.org/10.5194/cp-13-1023-2017.

Kaboth, S., Grunert, P., Lourens, L.J., 2017c. Mediterranean outflow water variability during the Early Pleistocene. PANGAEA. https://doi.org/10.1594/PANGAEA.871499.

Kano, A., Ferdelman, T.G., Williams, T., Henriet, J.-P., Ishikawa, T., Kawagoe, N., Takashima, C., Kakizaki, Y., Abe, K., Sakai, S., Browning, E.L., Li, X., 2007. Age constraints on the origin and growth history of a deep-water coral mound in the northeast Atlantic drilled during Integrated Ocean Drilling Program Expedition 307. Geology 35, 1051–1054. https://doi.org/10.1130/g23917a.1.

Khélifi, N., Frank, M., 2014. A major change in North Atlantic deep water circulation 1.6 million years ago. Clim. Past 10. https://doi.org/10.5194/cp-10-1441-2014.

Kirschvink, J.L., 1980. The least-squares line and plane and the analysis of paleomagnetic data. Geophys. J. Int. 62, 699–718. https://doi.org/10.1111/j.1365-246X.1980.tb02601.x.

Larrasoaña, J.C., Roberts, A.P., Rohling, E.J., Winklhofer, M., Wehausen, R., 2003. Three million years of monsoon variability over the northern Sahara. Climate Dynam. 21, 689–698. https://doi.org/10.1007/s00382-003-0355-z.

Laskar, J., Robutel, P., Joutel, F., Gastineau, M., Correia, A.C.M., Levrard, B., 2004. A long-term numerical solution for the insolation quantities of the Earth. Astron. Astrophys. 428, 261–285. https://doi.org/10.1051/0004-6361:20041335.

Lawrence, K.T., Herbert, T.D., Brown, C.M., Raymo, M.E., Haywood, A.M., 2009. High-amplitude variations in North Atlantic sea surface temperature during the early Pliocene warm period. Paleoceanography 24, PA2218. https://doi.org/10.1029/2008pa001669.

Lebreiro, S.M., Antón, L., Reguera, M.I., Fernández, M., Conde, E., Barrado, A.I., Yllera, A., 2015. Zooming into the Mediterranean outflow fossil moat during the 1.2–1.8 million years period (Early-Pleistocene) — an approach by radiogenic and stable isotopes. Global Planet. Change 135, 104–118. https://doi.org/10.1016/j.gloplacha.2015.10.010.

Lebreiro, S.M., Antón, L., Reguera, M.I., Marzocchi, A., 2018. Paleoceanographic and climatic implications of a new Mediterranean Outflow branch in the southern Gulf of Cadiz. Quat. Sci. Rev. 197, 92–111. https://doi.org/10.1016/j.quascirev.2018.07.036.

Lien, Ø.F., Hjelstuen, B.O., Zhang, X., Sejrup, H.P., 2022. Late Plio-Pleistocene evolution of the Eurasian Ice Sheets inferred from sediment input along the northeastern Atlantic continental margin. Quat. Sci. Rev. 282, 107433. https://doi.org/10.1016/j.quascirev.2022.107433.

Lisiecki, L.E., 2014. Atlantic overturning responses to obliquity and precession over the last 3 Myr. Paleoceanography 29. https://doi.org/10.1002/2013PA002505.

Lisiecki, L.E., Raymo, M., 2005. A Pliocene-Pleistocene stack of 57 globally distributed benthic $\delta^{18}O$ records. Paleoceanography 20, PA1003. https://doi.org/10.1029/2004PA001071.

Lofi, J., Voelker, A.H.L., Ducassou, E., Hernández-Molina, F.J., Sierro, F.J., Bahr, A., Galvani, A., Lourens, L.J., Pardo-Igúzquiza, E., Pezard, P., Rodríguez-Tovar, F.J., Williams, T., 2016. Quaternary chronostratigraphic framework and sedimentary processes for the Gulf of Cadiz and Portuguese Contourite Depositional Systems derived from Natural Gamma Ray records. Mar. Geol. 377, 40–57. https://doi.org/10.1016/j.margeo.2015.12.005.

Louarn, E., Morin, P., 2011. Antarctic intermediate water influence on Mediterranean Sea water outflow. Deep-Sea Res. I Oceanogr. Res. Pap. 58, 932–942. https://doi.org/10.1016/j.dsr.2011.05.009.

Lourens, L.J., Antonarakou, A., Hilgen, F.J., Van Hoof, A.A.M., Vergnaud-Grazzini, C., Zachariasse, W.J., 1996. Evaluation of the Plio-Pleistocene astronomical timescale. Paleoceanography 11, 391–413. https://doi.org/10.1029/96pa01125.

Marchitto, T.M., Curry, W.B., Lynch-Stieglitz, J., Bryan, S.P., Cobb, K.M., Lund, D.C., 2014. Improved oxygen isotope temperature calibrations for cosmopolitan benthic foraminifera. Geochim. Cosmochim. Acta 130, 1–11. https://doi.org/10.1016/j.gca.2013.12.034.

Maslin, M.A., Brierley, C.M., 2015. The role of orbital forcing in the Early Middle Pleistocene transition. Quat. Int. 389, 47–55. https://doi.org/10.1016/j.quaint.2015.01.047.

McCave, I.N., 2023. One million years of Mediterranean outflow strength. Quat. Sci. Rev. 317, 108260. https://doi.org/10.1016/j.quascirev.2023.108260.

McIntyre, A., Molfino, B., 1996. Forcing of Atlantic equatorial and subpolar millennial cycles by precession. Science 274, 1867–1870. https://doi.org/10.1126/science.274.5294.1867.

Miller, K.G., Mountain, G.S., Wright, J.D., Browning, J.V., 2011. A 180-million-year record of sea level and ice volume variations from continental margin and deep-sea isotopic records. Oceanography 24, 40–53. https://doi.org/10.5670/oceanog.2011.26.

Millot, C., 2014. Heterogeneities of in- and out-flows in the Mediterranean Sea. Prog. Oceanogr. 120, 254–278. https://doi.org/10.1016/j.pocean.2013.09.007.

Millot, C., Candela, J., Fuda, J.-L., Tber, Y., 2006. Large warming and salinification of the Mediterranean outflow due to changes in its composition. Deep-Sea Res. I Oceanogr. Res. Pap. 53, 656–666. https://doi.org/10.1016/j.dsr.2005.12.017.

Moal-Darrigade, P., Ducassou, E., Bout-Roumazeilles, V., Hanquiez, V., Perello, M.-C., Mulder, T., Giraudeau, J., 2022a. Source-to-sink pathways of clay minerals in the cadiz contourite system over the last 25 kyrs: the segregational role of mediterranean outflow water. Mar. Geol. 443, 106697. https://doi.org/10.1016/j.margeo.2021.106697.

Moal-Darrigade, P., Ducassou, E., Giraudeau, J., Bahr, A., Kaboth-Bahr, S., Hanquiez, V., Perello, M.-C., 2022b. MOW strengthening and contourite development over two analog climate cycles (MIS 12–11 and MIS 2–1) in the Gulf of Cadíz: an impact on North Atlantic climate during deglaciation V and MIS 11? Global Planet. Change 208, 103721. https://doi.org/10.1016/j.gloplacha.2021.103721.

Morée, A.L., Sun, T., Bretones, A., Straume, E.O., Nisancioglu, K., Gebbie, G., 2021. Cancellation of the precessional cycle in $\delta^{18}O$ records during the Early Pleistocene. Geophys. Res. Lett. 48. https://doi.org/10.1029/2020GL090035.

Moreno, A., Cacho, I., Canals, M., Grimalt, J.O., Sanchez-Goni, M.F., Shackleton, N., Sierro, F.J., 2005. Links between marine and atmospheric processes oscillating on a millennial time-scale. A multi-proxy study of the last 50,000 yr from the Alboran Sea (Western Mediterranean Sea). Quat. Sci. Rev. 24, 1623–1636.

Naafs, B.D.A., Hefter, J., Acton, G., Haug, G.H., Martinez-Garcia, A., Pancost, R., Stein, R., 2012. Strengthening of North American dust sources during the late Pliocene (2.7 Ma). Earth Planet. Sci. Lett. 317-318, 8–19. https://doi.org/10.1016/j.epsl.2011.11.026.

Nuber, S., Chalk, T., Ji, X., Scherrenberg, M., Heaton, T., Zhang, X., Stap, L., Trudgill, M., Block, H., Jian, Z., Xu, C., Kubota, K., Andersen, M., Barker, S., Yu, J., Foster, G., Rae, J., 2025. Mid Pleistocene Transition Caused by Decline in Atmospheric CO_2. Preprint deposited at ResearchSquare. https://doi.org/10.21203/rs.3.rs-6480074/v1.

Ogg, J.G., 2012. Geomagnetic polarity time scale. In: Gradstein, F.M., Ogg, J.G., Schmitz, M., Ogg, G. (Eds.), The Geologic Time Scale 2012. Elsevier, pp. 85–113.

Pierre, C., Belanger, P., Saliège, J.F., Urrutiaguer, M.J., Murat, A., 1999. Paleoceanography of the western Mediterranean during the Pleistocene: oxygen and carbon isotope records at Site 975. In: Zahn, R., Comas, M.C., Klaus, A. (Eds.), Proceedings ODP, Scientific Results. Ocean Drilling Program, College Station, TX, pp. 481–488.

Pierre, C., Belanger, P., Saliège, J.F., Urrutiaguer, M.J., 2020. Globigerina bulloides stable and carbon oxygen isotope record of ODP Site 161-975. PANGAEA. https://doi.org/10.1594/PANGAEA.911743.

Raddatz, J., Rüggeberg, A., Liebetrau, V., Foubert, A., Hathorne, E.C., Fietzke, J., Eisenhauer, A., Dullo, W.-C., 2014. Environmental boundary conditions of cold-water coral mound growth over the last 3 million years in the Porcupine Seabight, Northeast Atlantic. Deep-Sea Res. II Top. Stud. Oceanogr. 99, 227–236. https://doi.org/10.1016/j.dsr2.2013.06.009.

Raffi, I., Backman, J., Fornaciari, E., Pälike, H., Rio, D., Lourens, L., Hilgen, F., 2006. A review of calcareous nannofossil astrobiochronology encompassing the past 25 million years. Quat. Sci. Rev. 25, 3113–3137. https://doi.org/10.1016/j.quascirev.2006.07.007.

Raffi, I., Wade, B.S., Pälike, H., Beu, A.G., Cooper, R., Crundwell, M.P., Krijgsman, W., Moore, T., Raine, I., Sardella, R., Vernyhorova, Y.V., 2020. Chapter 29 - the neogene period. In: Gradstein, F.M., Ogg, J.G., Schmitz, M.D., Ogg, G.M. (Eds.), Geologic Time Scale 2020. Elsevier, pp. 1141–1215. https://doi.org/10.1016/B978-0-12-824360-2.00029-2.

Raymo, M.E., Nisancioglu, K.H., 2003. The 41 kyr world: Milankovitch's other unsolved mystery. Paleoceanography 18, 11–16. https://doi.org/10.1029/2002PA000791.

Raymo, M.E., Oppo, D.W., Flower, B.P., Hodell, D.A., McManus, J.F., Venz, K.A., Kleiven, K.F., McIntyre, K., 2004. Stability of North Atlantic water masses in face of pronounced climate variability during the Pleistocene. Paleoceanography 19, PA2008. https://doi.org/10.1029/2003PA000921.

Raymo, M.E., Lisiecki, L.E., Nisancioglu, K.H., 2006. Plio-Pleistocene ice volume, Antarctic climate, and the global $\delta^{18}O$ record. Science 313, 492–495. https://doi.org/10.1126/science.1123296.

Reagan, J.R., Boyer, T.P., García, H.E., Locarnini, R.A., Baranova, O.K., Bouchard, C., Cross, S.L., Mishonov, A.V., Paver, C.R., Seidov, D., Wang, Z., Dukhovskoy, D., 2024. World Ocean Atlas 2023. NOAA National Centers for Environmental Information.

Revel, M., Ducassou, E., Grousset, F.E., Bernasconi, S.M., Migeon, S., Revillon, S., Mascle, J., Murat, A., Zaragosi, S., Bosch, D., 2010. 100,000 years of African monsoon variability recorded in sediments of the Nile margin. Quat. Sci. Rev. 29, 1342–1362. https://doi.org/10.1016/j.quascirev.2010.02.006.

Rogerson, M., Bigg, G., Rohling, E., Ramirez, J., 2012a. Vertical density gradient in the eastern North Atlantic during the last 30,000 years. Climate Dynam. 39, 589–598. https://doi.org/10.1007/s00382-011-1148-4.

Rogerson, M., Rohling, E.J., Bigg, G.R., Ramirez, J., 2012b. Paleoceanography of the Atlantic-Mediterranean exchange: overview and first quantitative assessment of climatic forcing. Rev. Geophys. 50, RG2003. https://doi.org/10.1029/2011rg000376.

Rohling, E.J., Foster, G.L., Grant, K.M., Marino, G., Roberts, A.P., Tamisiea, M.E., Williams, F., 2014. Sea-level and deep-sea-temperature variability over the past 5.3 million years. Nature 508, 477–482. https://doi.org/10.1038/nature13230.

Rohling, E.J., Marino, G., Grant, K.M., 2015. Mediterranean climate and oceanography, and the periodic development of anoxic events (sapropels). Earth Sci. Rev. 143, 62–97. https://doi.org/10.1016/j.earscirev.2015.01.008.

Roque, C., Duarte, H., Terrinha, P., Valadares, V., Noiva, J., Cachão, M., Ferreira, J., Legoinha, P., Zitellini, N., 2012. Pliocene and Quaternary depositional model of the Algarve margin contourite drifts (Gulf of Cadiz, SW Iberia): Seismic architecture, tectonic control and paleoceanographic insights. Mar. Geol. 303–306, 42–62. https://doi.org/10.1016/j.margeo.2011.11.001.

Roque, D., Parras-Berrocal, I., Bruno, M., Sánchez-Leal, R., Hernández-Molina, F.J., 2019. Seasonal variability of intermediate water masses in the Gulf of Cádiz: implications of the Antarctic and subarctic seesaw. Ocean Sci. 15, 1381–1397. https://doi.org/10.5194/os-15-1381-2019.

Rossignol-Strick, M., Nesteroff, V., Olive, P., Vergnaud-Grazzini, C., 1982. After the deluge: Mediterranean stagnation and sapropel formation. Nature 295, 105–110.

Rossignol-Strick, M., Paterne, M., Bassinot, F.C., Emeis, K.C., De Lange, G.J., 1998. An unusual mid-Pleistocene monsoon period over Africa and Asia. Nature 392, 269–272. https://doi.org/10.1038/32631.

Ruddiman, W.F., Raymo, M.E., Martinson, D.G., Clement, B.M., Backman, J., 1989. Pleistocene evolution: Northern Hemisphere ice sheets and North Atlantic Ocean. Paleoceanography 4, 353–412.

Rutherford, S., D'Hondt, S., 2000. Early onset and tropical forcing of 100,000-year Pleistocene glacial cycles. Nature 408, 72–75. https://doi.org/10.1038/35040533.

Sakai, S., Kano, A., Abe, K., 2009. Origin, glacial-interglacial responses, and controlling factors of a cold-water coral mound in NE Atlantic. Paleoceanography 24. https://doi.org/10.1029/2008PA001695.

Schlitzer, R., 2025. Ocean Data View. odv.awi.de.

Schönfeld, J., 2006. Taxonomy and distribution of the *Uvigerina peregrina* plexus in the tropical to northeastern Atlantic. J. Foraminifer. Res. 36, 355–367.

Schönfeld, J., Altenbach, A.V., 2005. Late Glacial to recent distribution pattern of deep-water Uvigerina species in the north-eastern Atlantic. Mar. Micropaleontol. 57, 1–24.

Schroeder, K., Chiggiato, J., Josey, S.A., Borghini, M., Aracri, S., Sparnocchia, S., 2017. Rapid response to climate change in a marginal sea. Sci. Rep. 7, 4065. https://doi.org/10.1038/s41598-017-04455-5.

Shackleton, N.J., 1974. Attainment of isotopic equilibrium between ocean water and the benthonic foraminifera genus Uvigerina: isotopic changes in the ocean during the last Glacial. Colloques Int. du C.N.R.S. 219, 203–209.

Sierro, F.J., Ledesma, S., Flores, J.-A., Torrescusa, S., del Olmo, W.M., 2000. Sonic and gamma-ray astrochronology: cycle to cycle calibration of Atlantic climatic records to Mediterranean sapropels and astronomical oscillations. Geology 28, 695–698. https://doi.org/10.1130/0091-7613(2000)28<695:sagact>2.0.co;2.

Sierro, F.J., Hodell, D.A., Andersen, N., Azibeiro, L.A., Jimenez-Espejo, F.J., Bahr, A., Flores, J.A., Ausin, B., Rogerson, M., Lozano-Luz, R., Lebreiro, S.M., Hernandez-Molina, F.J., 2020. Mediterranean overflow over the last 250 kyr: freshwater forcing from the tropics to the ice sheets. Paleoceanogr. Paleoclimatol. 35, e2020PA003931. https://doi.org/10.1029/2020PA003931.

Sierro, F.J., Jimenez-Espejo, F.J., Tarruella, J.P., Hodell, D.A., 2025. Atlantic Atmospheric Rivers and the Pulse of Deep Mediterranean Respiration. Preprint deposted at ResearchSquare. https://doi.org/10.21203/rs.3.rs-5678981/v1.

Singh, A.D., Rai, A.K., Tiwari, M., Naidu, P.D., Verma, K., Chaturvedi, M., Niyogi, A., Pandey, D., 2015. Fluctuations of Mediterranean Outflow Water circulation in the Gulf of Cadiz during MIS 5 to 7: evidence from benthic foraminiferal assemblage and stable isotope records. Global Planet. Change 133, 125–140. https://doi.org/10.1016/j.gloplacha.2015.08.005.

Stow, D.A.V., Faugères, J.C., 2008. Chapter 13 contourite facies and the facies model. In: Rebesco, M., Camerlenghi, A. (Eds.), Developments in Sedimentology. Elsevier, pp. 223–256.

Stow, D.A.V., Hernández-Molina, F.J., Alvarez Zarikian, C.A., the.Expedition.339. Scientists, 2013. Proceedings IODP exp. 339 - Mediterranean outflow. In: Stow, D.A.V., Hernández-Molina, F.J., Alvarez Zarikian, C.A., the Expedition 339 Scientists (Eds.), Book Proceedings IODP Exp. 339 - Mediterranean Outflow. Integrated Ocean Drilling Program Management International, Inc, Tokyo. https://doi.org/10.2204/iodp.proc.339.2013.

The Cenozoic CO_2 Proxy Integration Project Consortium, Hönisch, B., Royer, D.L., Breecker, D.O., Polissar, P.J., Bowen, G.J., Henehan, M.J., Cui, Y., Steinthorsdottir, M., McElwain, J.C., Kohn, M.J., Pearson, A., Phelps, S.R., Uno, K.T., Ridgwell, A., Anagnostou, E., Austermann, J., Badger, M.P.S., Barclay, R.S., Bijl, P. K., Chalk, T.B., Scotese, C.R., de la Vega, E., DeConto, R.M., Dyez, K.A., Ferrini, V., Franks, P.J., Giulivi, C.F., Gutjahr, M., Harper, D.T., Haynes, L.L., Huber, M., Snell, K.E., Keisling, B.A., Konrad, W., Lowenstein, T.K., Malinverno, A., Guillermic, M., Mejía, L.M., Milligan, J.N., Morton, J.J., Nordt, L., Whiteford, R., Roth-Nebelsick, A., Rugenstein, J.K.C., Schaller, M.F., Sheldon, N.D., Sosdian, S., Wilkes, E.B., Witkowski, C.R., Zhang, Y.G., Anderson, L., Beerling, D.J., Bolton, C., Cerling, T.E., Cotton, J.M., Da, J., Ekart, D.D., Foster, G.L., Greenwood, D.R., Hyland, E.G., Jagniecki, E.A., Jasper, J.P., Kowalczyk, J.B., Kunzmann, L., Kürschner, W.M., Lawrence, C.E., Lear, C.H., Martínez-Botí, M.A., Maxbauer, D.P., Montagna, P., Naafs, B.D.A., Rae, J.W.B., Raitzsch, M., Retallack, G.J., Ring, S.J., Seki, O., Sepúlveda, J., Sinha, A., Tesfamichael, T.F., Tripati, A., van der Burgh, J., Yu, J., Zachos, J.C., Zhang, L., 2023. Toward a Cenozoic history of atmospheric CO_2. Science 382, eadi5177. https://doi.org/10.1126/science.adi5177.

Thierens, M., Browning, E., Pirlet, H., Loutre, M.F., Dorschel, B., Huvenne, V.A.I., Titschack, J., Colin, C., Foubert, A., Wheeler, A.J., 2013. Cold-water coral carbonate mounds as unique palaeo-archives: the Plio-Pleistocene Challenger Mound record

(NE Atlantic). Quat. Sci. Rev. 73, 14–30. https://doi.org/10.1016/j.quascirev.2013.05.006.

Tiedemann, R., Sarnthein, M., Shackleton, N.J., 1994. Astronomic timescale for the Pliocene Atlantic $\delta^{18}O$ and dust flux records of Ocean Drilling Program site 659. Paleoceanography 9, 619–638.

Toucanne, S., Jouet, G., Ducassou, E., Bassetti, M.-A., Dennielou, B., Angue Minto'o, C. M., Lahmi, M., Touyet, N., Charlier, K., Lericolais, G., Mulder, T., 2012. A 130,000-year record of Levantine Intermediate Water flow variability in the Corsica Trough, western Mediterranean Sea. Quat. Sci. Rev. 33, 55–73. https://doi.org/10.1016/j.quascirev.2011.11.020.

Trotta, S., Duque-Castaño, M., Rodrigues, T., Voelker, A.H.L., Maiorano, P., Balestra, B., Flores, J.-A., Siniscalchi, A., Addante, M., Marino, M., 2025. High-frequency glacial climate instability during the early Pleistocene: insights from IODP site U1387 (Gulf of Cadiz). Palaeogeogr. Palaeoclimatol. Palaeoecol. 674, 113041. https://doi.org/10.1016/j.palaeo.2025.113041.

Voelker, A.H.L., Lebreiro, S.M., Schönfeld, J., Cacho, I., Erlenkeuser, H., Abrantes, F., 2006. Mediterranean outflow strengthening during northern hemisphere coolings: a salt source for the glacial Atlantic? Earth Planet. Sci. Lett. 245, 39–55. https://doi.org/10.1016/j.epsl.2006.03.014.

Voelker, A.H.L., Colman, A., Olack, G., Waniek, J.J., Hodell, D., 2015a. Oxygen and hydrogen isotope signatures of Northeast Atlantic water masses. Deep-Sea Res. II Top. Stud. Oceanogr. 116, 89–106. https://doi.org/10.1016/j.dsr2.2014.11.006.

Voelker, A.H.L., Colman, A.S., Olack, G., Waniek, J.J., Hodell, D.A., 2015b. Physical oceanography during EUROFLEETS Iberia-Forams. PANGAEA. https://doi.org/10.1594/PANGAEA.831461.

Voelker, A.H.L., Salgueiro, E., Rodrigues, T., Jimenez-Espejo, F.J., Bahr, A., Alberto, A., Loureiro, I., Padilha, M., Rebotim, A., Röhl, U., 2015c. Mediterranean outflow and surface water variability off southern Portugal during the early Pleistocene: a snapshot at marine isotope stages 29 to 34 (1020–1135 ka). Global Planet. Change 133, 223–237. https://doi.org/10.1016/j.gloplacha.2015.08.015.

Voelker, A.H.L., Jimenez-Espejo, F.J., Bahr, A., Rebotim, A., Cavaleiro, C., Salgueiro, E., Röhl, U., 2018. Data report: IODP Site U1387: the revised splice between Sections U1387B-18X-3 and U1387C-8R-3 (>171.6 mcd). In: Stow, D.A.V., Hernández-Molina, F.J., Alvarez Zarikian, C.A., the Expedition 339 Scientists (Eds.), Proceedings of the Integrated Ocean Drilling Program, 339. Integrated Ocean Drilling Program Management International, Inc, Tokyo, pp. 1–11. https://doi.org/10.2204/iodp.proc.339.204.2018.

Voelker, A.H.L., Rodrigues, T., Trotta, S., Marino, M., Kuhnert, H., 2022. A Southern Portuguese margin perspective of marine isotope stage 47 – an interglacial in the 41 kyr world. Atmosphere 13, 1378. https://doi.org/10.3390/atmos13091378.

Wang, P., Tian, J., Lourens, L.J., 2010. Obscuring of long eccentricity cyclicity in Pleistocene oceanic carbon isotope records. Earth Planet. Sci. Lett. 290, 319–330. https://doi.org/10.1016/j.epsl.2009.12.028.

Yan, Y., Bender, M.L., Brook, E.J., Clifford, H.M., Kemeny, P.C., Kurbatov, A.V., Mackay, S., Mayewski, P.A., Ng, J., Severinghaus, J.P., Higgins, J.A., 2019. Two-million-year-old snapshots of atmospheric gases from Antarctic ice. Nature 574, 663–666. https://doi.org/10.1038/s41586-019-1692-3.